Robust Eigen-Filter Design for Ultrasound Flow Imaging Using a Multivariate Clustering Technique

by

Saad Ahmed Waraich

A thesis
presented to the University of Waterloo
in fulfillment of the
thesis requirement for the degree of
Master of Applied Science
in
Electrical and Computer Engineering

Waterloo, Ontario, Canada, 2019

Author's Declaration

I hereby declare that I am the sole author of this thesis. This is a true copy of the thesis, including any required final revisions, as accepted by my examiners.

I understand that my thesis may be made electronically available to the public.

Abstract

Blood flow visualization is a challenging task in the presence of tissue motion. Unsuppressed tissue clutter produces flashing artefacts in ultrasound flow imaging which hampers blood flow detection by dominating part of the blood flow signal in certain challenging clinical imaging applications, ranging from cardiac imaging (maximal tissue vibrations) to microvascular flow imaging (very low blood flow speeds). Conventional clutter filtering techniques perform poorly since blood and tissue clutter echoes share similar spectral characteristics. Eigen-based filtering was recently introduced and has shown good clutter rejection performance; however, flow detection performance in eigen filtering suffers if tissue and flow signal subspaces overlap after eigen components are projected to a single signal feature space for clutter rank selection.

To address this issue, a novel multivariate clustering based singular value decomposition (SVD) filter design is developed. The proposed multivariate clustering based filter robustly detects and removes non-blood eigen components by leveraging on three key spatiotemporal statistics: singular value magnitude, spatial correlation and the mean Doppler frequency of singular vectors. A better clutter suppression framework is necessary for high-frame-rate (HFR) ultrasound imaging since it is more susceptible to tissue motion due to poorer spatial resolution (tissue clutter bleeds into flow pixels easily). Hence, to test the clutter rejection performance of the proposed filter, HFR plane wave data was acquired from an *in vitro* flow phantom testbed and *in vivo* from a subject's common carotid artery and jugular vein region induced with extrinsic tissue motion (voluntary probe motion). The proposed method was able to adaptively detect and preserve blood eigen components and enabled fully automatic identification of eigen-components corresponding to tissue clutter, blood and noise that removes dependency on the operator for optimal rank selection.

The flow detection efficacy of the proposed multivariate clustering based SVD filter was statistically evaluated and compared with current clutter rank estimation methods using the receiver operating characteristic (ROC) analysis. Results for both *in vitro* and *in vivo* experiments showed that the multivariate clustering based SVD filter yielded the highest area under the ROC curve at both peak systole (0.98 for *in vitro*; 0.95 for *in vivo*) and end diastole (0.96 for *in vitro*; 0.93 for *in vivo*) in comparison with other clutter rank estimation methods, signifying its improved flow detection capability. The impact of this work is on the automated as well as adaptive (in contrast to a fixed cut-off) selection of eigen-components which can potentially allow to overcome the flow detection challenges associated with fast tissue motion in cardiovascular imaging and slow flow in microvascular imaging which is critical for cancer diagnoses.

Acknowledgements

The fusion of medical science and engineering is something I am genuinely intrigued about, and this enthusiasm brought me towards the LITMUS lab at the University of Waterloo. The journey was challenging but an amazing learning experience, and I am very grateful to all those who helped and made it easier for me to achieve my goals.

First, I would like to take this opportunity to thank my supervisor, Prof. Alfred Yu, to offer me the chance to study at the University of Waterloo and for his continued patience and guidance to make me become a better researcher and harness my full potential.

I would also like to thank all my lab colleagues, especially Adrian Chee and Billy Yiu that helped me immensely throughout my degree with their knowledge, experience and sheer kindness. To all my other lab colleagues and friends, I will always cherish the time spent working and learning with you all. Will really miss all the fun activities we were part of together.

I cannot thank my parents enough for their moral and spiritual support all the time, to ensure I stay well motivated and continue to tread the path of academic success.

Table of Contents

List of Figures

List of Tables

List of Abbreviations

Abbreviations

ADC	Analog-to-digital converter
AUC	Area under the curve
B-mode	Brightness-mode
BMF	Blood-mimicking fluid
CCA	Common carotid artery
EMD	Empirical mode decomposition
FAR	False alarm rate
GMM	Gaussian mixture model
HFR	High-frame-rate
JV	Jugular vein
PRF	Pulse repetition frequency
PLA	Polylactic acid
PVA	Polyvinyl alcohol
ROC	Receiver operating characteristic
RF	Radio frequency
SNR	Signal-to-noise ratio
SVD	Singular value decomposition
SSM	Spatial similarity matrix
TPR	True positive rate
2-D	Two-dimensional
3-D	Three-dimensional

List of Symbols

Imaging Parameters

C_0	Speed of sound
f_{DAQ}	Effective data acquisition rate
f_{PRF}	Pulse repetition frequency
f_t	Transmission frequency
f_r	Received frequency
v	Scatterer velocity
θ	Beam-flow angle

Signal and Image Processing Parameters

C	Spatial correlation vector
D	Diagonal matrix
$\hat{\boldsymbol{f}}_{\boldsymbol{k}}$	Mean Doppler frequency estimate for kth singular vector
N_t	Size of slow-time ensemble
N_x	Size of lateral dimension
N_z	Size of depth dimension
$PD(x, z)$	Post-filtered power Doppler image matrix
$\boldsymbol{S}$	Casorati matrix
s(x, z, t)	Raw data matrix
t	Slow-time ensemble dimension
U	Left singular vector
$\mathbf{U_k}$	Kth left singular vector
$\overline{\mathbf{U_k}}$	Mean of kth left singular vector
V	Right singular vector
$\mathbf{V_k}$	Kth right singular vector
x	Lateral dimension
z	Depth dimension
λ_k	Singular values from diagonal matrix
$\boldsymbol{\sigma_k}$	Standard deviation of the kth left singular vector

Chapter 1 Introduction

1.1 Chapter Overview

Ultrasound imaging has established itself as a mature screening and diagnostic imaging modality in clinical practice. In fact, ultrasound is being used in at least a quarter of all imaging procedures globally (Wells, 2006). The breakthrough in high-frame-rate (HFR) ultrasound imaging has enabled several novel clinical applications (Tanter & Fink, 2014). Although research in the ultrasound imaging field has progressed rapidly, knowledge of conventional ultrasound principles is still important to establish a strong foundation. Hence, Section 1.2 explains the fundamental physical and flow estimation principles behind ultrasound imaging. Next, the HFR imaging scheme is introduced followed by a background of the tissue motion based clutter problem encountered in ultrasound flow imaging. Limitations of the conventional and current methods of clutter filtering are detailed later and in the last section the motivation, hypothesis and objectives of this research work are outlined.

1.2 Background

1.2.1 Physical Principles of Ultrasound Imaging

Ultrasound imaging is generally done by placing a piezo-electric transducer on the skin that transmits sound waves with high center frequencies (typically ranging from 2-15 MHz) and then receives the back-scattered echoes from body tissues. The received signal consists of the emitted pulse which is reflected as it crosses the boundary of media with an acoustic impedance mismatch (Jensen J. A., Medical ultrasound imaging, 2007). The speed of sound (c_0) in human body tissues is typically 1540 m/s. Using this speed, the depth of the returned echoes can be computed using their time of flight. As the ultrasound waves pass through the soft tissues, part of it is reflected due to different types of reflection: Rayleigh scattering, specular reflection and backscattering. At typical ultrasound frequencies, the scattering produced by the red blood cells is Rayleigh scattering which happens when

the scatterer size is smaller than the ultrasound wavelength. The received echoes are then converted into voltage signals using an analog-to-digital converter (ADC), which outputs the radio frequency (RF) signal for processing. A brightness-mode (B-mode) image is generated by rendering the received ultrasound RF signals as bright dots across 2-D space. The brightness of each dot is a function of the returned echo signal amplitude.

1.2.2 Flow Estimation Principles in Ultrasound Imaging

Flow estimation in ultrasound imaging is based on pulsed-wave Doppler technique, in which RF signal acquisitions are compared between at least two subsequent firings to find spatial displacement of the scatterers over a time interval. Fig. 1.1 illustrates this technique by showing a scatterer in upward motion that will cause a change in the pulse-echo time of flight between two time intervals. The echo received from the second firing will arrive earlier in comparison to the first firing as the distance between the ultrasound transducer and the scatterer is reduced. The set of RF signals obtained from the subsequent firings is called a slow-time ensemble, and the number of firings in each slow-time ensemble is called the ensemble size.

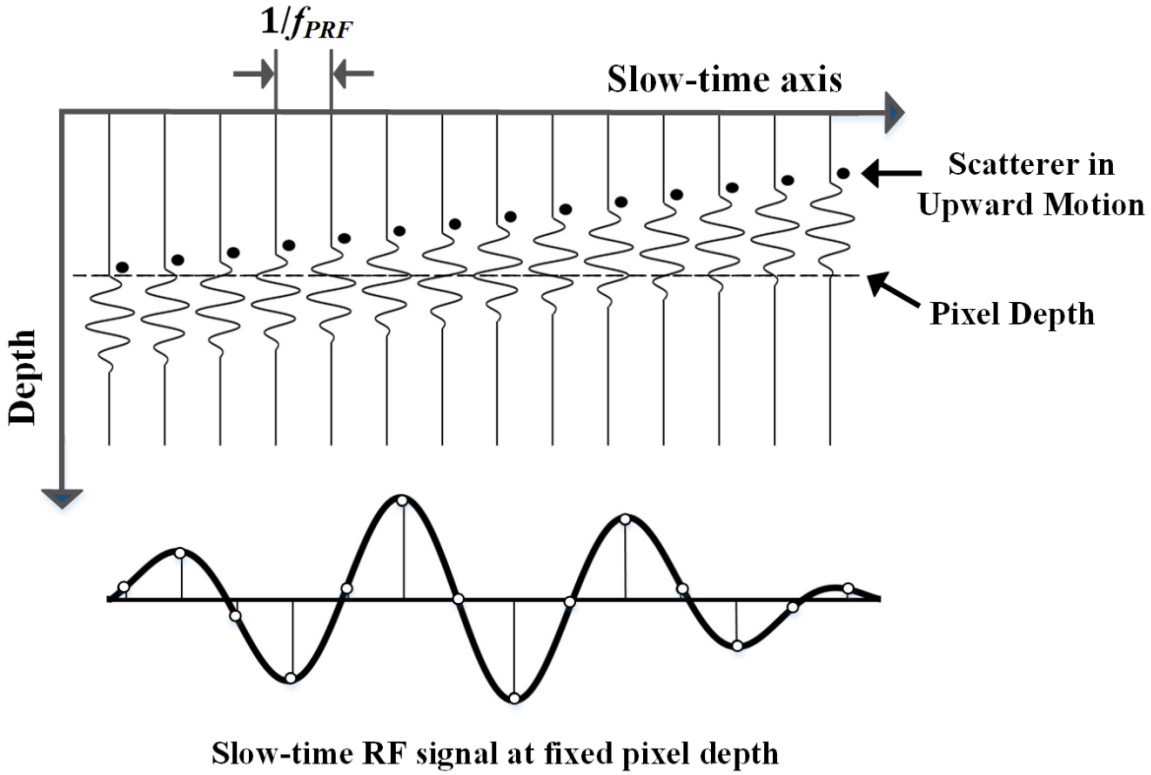

Fig. 1.1. Flow estimation in ultrasound based on pulsed-wave Doppler principle. The received RF echoes from the backscattering of the scatterer at each firing is sampled at a fixed depth position. Velocity of the scatterer can be estimated from the changes in phase of the sampled slow-time signal.

The flow velocity of this scatterer can be estimated by the following Doppler equation:

$$v = \frac{(f_t - f_r)C_0}{2f_t \cos\theta} \tag{1-1}$$

Where v is the scatterer velocity, f_t is the ultrasound transmission frequency, f_r is the received frequency and θ is the beam-flow angle (angle between the ultrasound beam axis and the direction of scatterer motion, i.e., the flow direction). It is worth noting that the change in phase is the quantity essentially being measured for flow estimation instead of the frequency shift. The frequency shift in one pulse is equivalent to the phase shift from one pulse to the next.

1.2.3 High-frame-rate Data Acquisition Technique

In conventional ultrasound imaging scanners, focused beams are fired line by line to insonify the entire imaging view as shown in Fig 1.2(a). Each scan line acquisition is coherently summed to form a single B-mode image. Such a transmission scheme leads to a limited frame rate of about 30 to 40 Hz, without sacrificing the number of scan lines (Montaldo, Tanter, Bercoff, Benech, & Fink, 2009). The use of line by line scanning also limits the number of temporal samples (ensemble size) that are acquired at a scan line before the system moves on to the next one.

Over the past two decades, high-frame-rate ultrasound based on unfocused plane wave transmission (Tanter, Bercoff, Sandrin, & Fink, 2002) (Udesen, Gran, & Jensen, 2005) has allowed more than a 100-folds increase in frame rate. As illustrated in Fig 1.2(b), instead of focused beam firings, all the transducer elements are fired at the same time to generate plane waves which cover the entire imaging view. A single plane wave transmit can be used to form an image, but since plane waves are unfocused the resultant images will suffer from a poor signal-to-noise ratio (SNR) and be of low-resolution. The solution to this problem is to transmit plane waves at different steering angles (angle between the depth direction and the beam-axis) as shown in Fig 1.2(c) and coherently sum the low-resolution images to yield a high-resolution compounded image with improved SNR (Montaldo et al., 2009). For N Tx angles, the effective data acquisition rate (f_{DAQ}) is given by f_{PRF}/N, where f_{PRF} is the ultrasound pulse repetition frequency (PRF). The compromise in this multi-angle plane wave compounding approach is a loss in contrast compared to the conventional focused beam firings method where the pressure field at the focal depth is much higher, resulting in better SNR.

Apart from plane wave based ultrasound imaging, spherical waves can also be transmitted for broad-field imaging (Ylitalo & Ermert, 1994), (Jensen, Nikolov, Gammelmark, & Pedersen, 2006). This approach is known as synthetic aperture imaging, where each transducer element is activated one by one to transmit a spherical wave that insonifies the entire imaging view. The echo from each

emission is received using all elements. It yields a single low-resolution image and multiple low-resolution images formed are compounded to generate a synthetic image, also known as a high-resolution image, as illustrated in Fig. 1.3. Therefore, the acquisition rate for this synthetic aperture transmission scheme is f_{DAQ} is equal to f_{PRF}/M, where M is the total number of emissions.

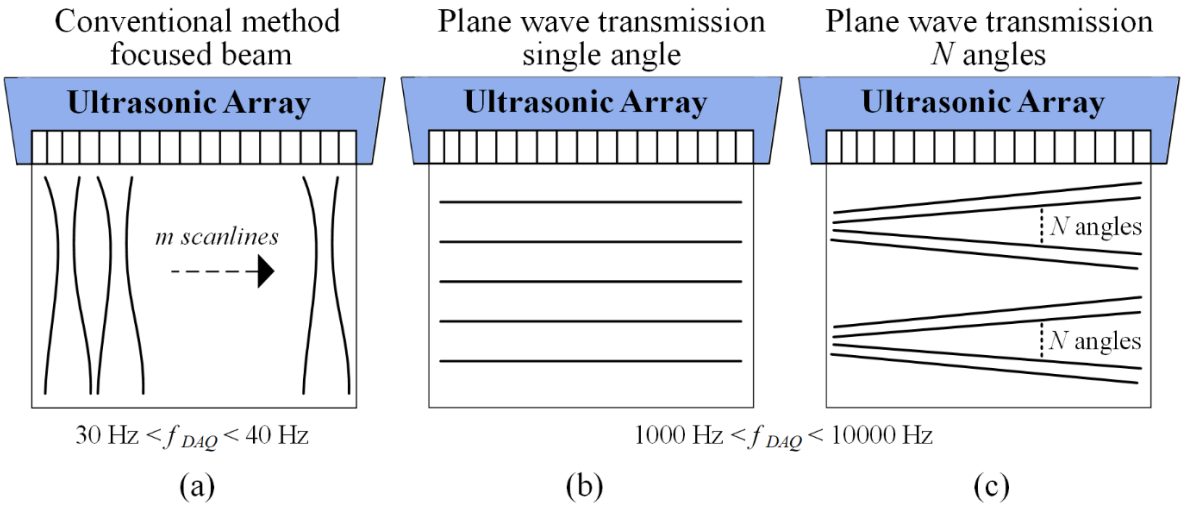

Fig. 1.2. (a) Conventional focused beam based ultrasound imaging in which m scanlines are merged to form an image. High-frame-rate data acquisition based on plane wave transmissions with (b) single steering angle, and (c) multiple N angles.

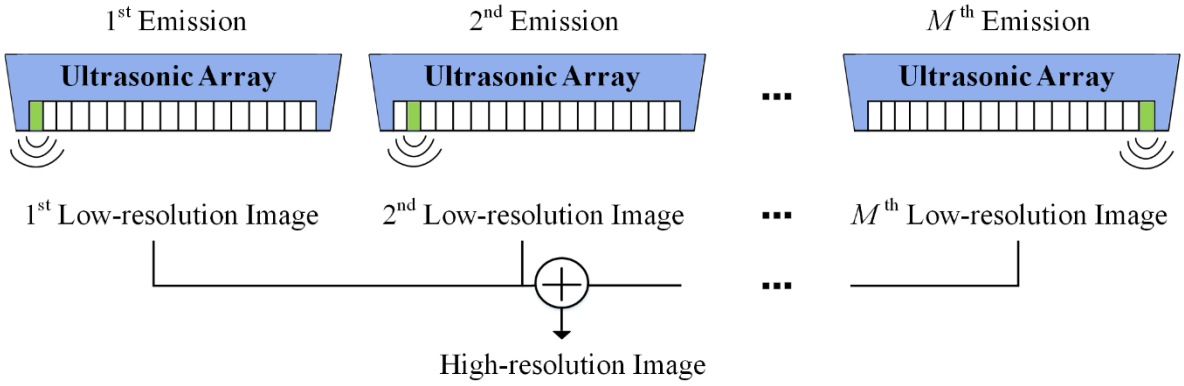

Fig. 1.3. High-frame-rate data acquisition using synthetic aperture imaging method. Spherical waves are emitted by a single transducer element. M low-resolution images are compounded to form a single high-resolution image.

1.2.4 Origin of Clutter in Ultrasound

Clutter is defined as unwanted echoes produced by stationary or slow moving tissue structures like pulsating vessel walls, muscular tissue vibrations and heart valve pulsations (Jensen J. , 1993). As illustrated in Fig. 1.4(a), in focused scan line based ultrasound imaging, clutter artifact emerges from the grating lobes of linear transducer arrays which reflect from tissue structures that are outside of the main ultrasound beam in the non-blood regions (Paul, Barthez, DVM, Peter, & Scrivani, 1997). Hence, tissue clutter echoes produced by the grating lobes are displayed along the axis of the main lobe positioned in the flow region. In high-frame-rate ultrasound imaging, since a plane wave is used to excite the entire imaging view at the same instant, clutter echoes from static and slowly moving tissues corrupt the blood flow signal even more. Fig. 1.4(b) shows that during receive delay-and-sum beamforming where the transit time of echoes received by each array element are computed, tissue clutter and blood flow echoes can have the same transit time based on their similar shortest distance to the array element. This way echoes from tissue clutter get beamformed with the blood echoes and result in corruption of the flow signal.

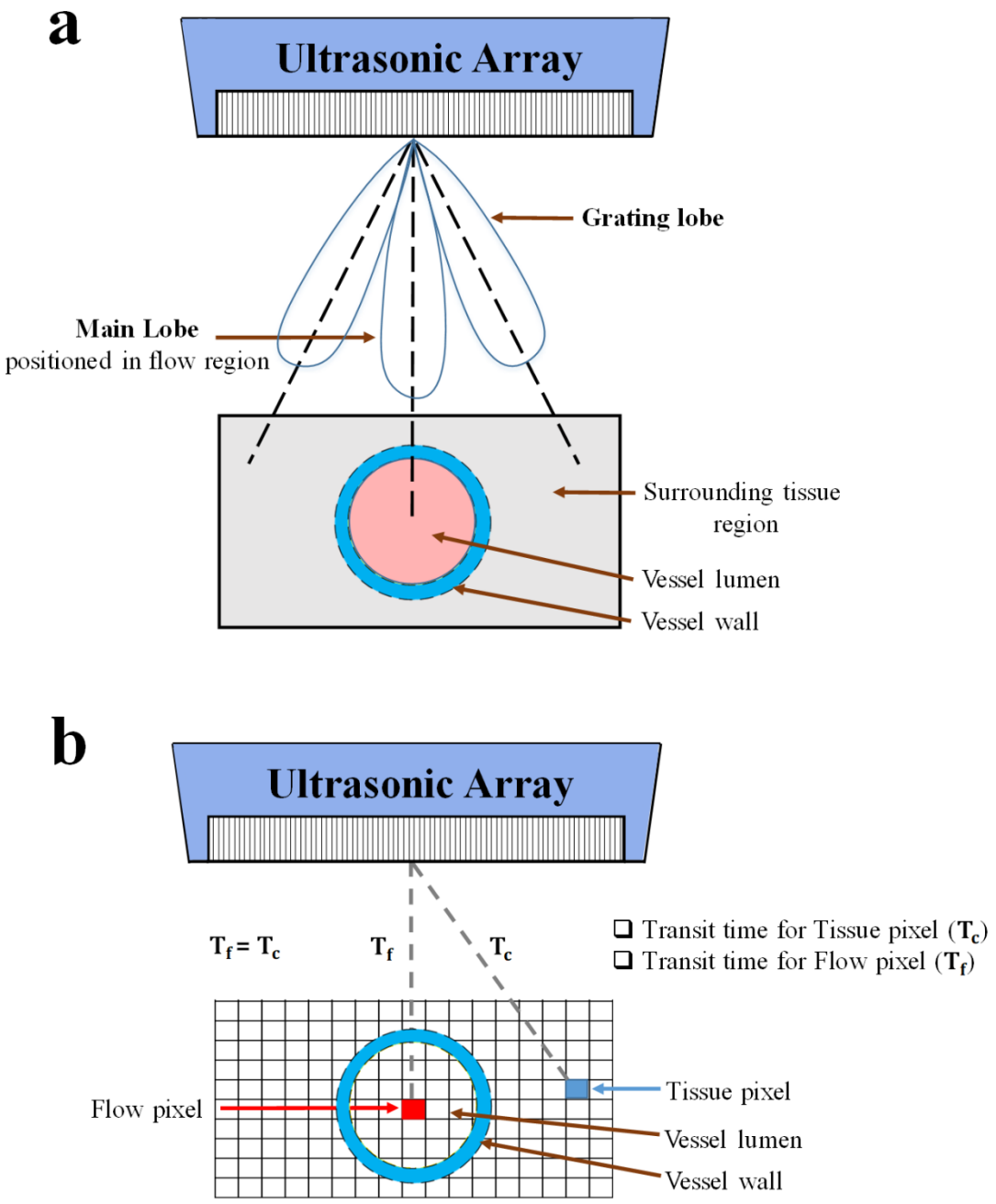

Fig 1.4. Illustration of how tissue clutter is generated in (a) conventional focused beam based ultrasound imaging where grating lobes reflect sound from tissue structures outside flow region (b) High-frame-rate plane wave imaging approach where tissue clutter gets beamformed with the blood signal due to similar transit time of echoes from both tissue and blood pixels.

1.2.5 Tissue Motion in Ultrasound Flow Imaging

Tissue clutter hampers blood flow detection in ultrasound flow imaging since the backscattering strength of tissue is much stronger than blood due to its higher acoustic impedance mismatch (Bjaerum, Torp, & Kristoffersen, 2002). Moreover, tissue motion being relatively slower than blood dominates low frequencies compared to the fast fluctuations of the blood flow signal that exhibit a higher range of frequencies (Hoskins & McDicken, 1997). As shown in Fig. 1.5(a), in the presence of tissue motion, clutter echoes become broadband and overlap the slower blood flow signal (Heimdal & Torp, 1997). This problem of tissue and blood echoes sharing similar spectral characteristics is found in important ultrasound (US) imaging applications. Such as, imaging flow with fast vessel wall motion is a major challenge in cardiac imaging (Mozumi & Hasegawa, 2019), (Takahashi, Hasegawa, & Kanai, June 2015). Furthermore, when detecting slow flow in tumor microvasculature which is critical for cancer diagnoses (Jin, He, Wu, Lin, & Jiang, 2016), (Bayat, Fatemi, & Alizad, 2018), the blood frequencies in this case become much closer to tissue clutter as shown in Fig. 1.5(b).

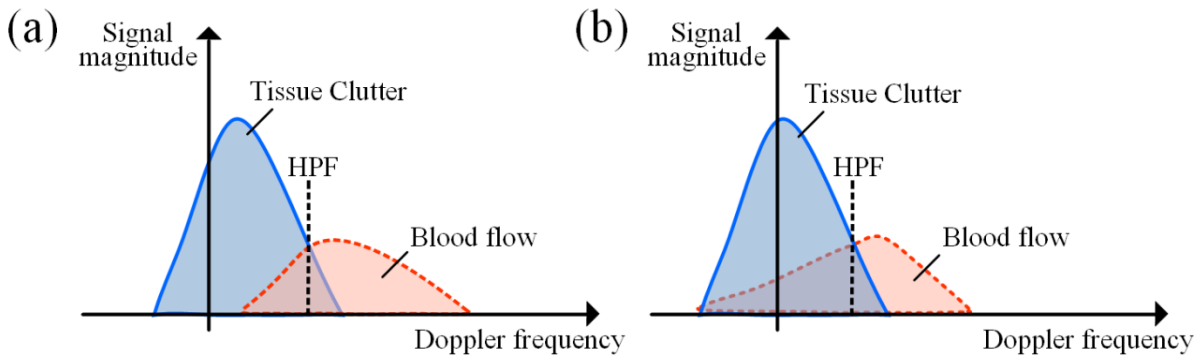

Fig. 1.5. Frequency spectrum of tissue clutter and blood flow signal with high-pass filter (HPF) cut-off indicated with a dashed line at scenarios with (a) fast tissue motion and fast flow (b) slow flow in microvasculature and insignificant tissue motion.

1.2.6 Conventional Methods of Clutter Filtering

Conventionally, high-pass filtering methods like the finite impulse response (FIR) filter (Jensen J. , 1993), infinite impulse response (IIR) filters (Hoeks, Vorst, Dabekaussen, Brands, & Reneman, 1991) and polynomial regression filters (Kadi & Loupas, 1995) have been used to remove low frequency tissue clutter. However, since these methods are limited to the temporal dimension only, they fail to discriminate between tissue and blood signals when their Doppler frequency spectrums overlap significantly. Hence, temporal filtering techniques cannot reject tissue clutter without loss of lower velocity blood flow as illustrated in Fig. 1.5(a), (b). Inadequate suppression of tissue clutter introduces bias in the velocity estimates, thereby altering the blood flow velocity profile. Adaptive filters based on clutter downmixing have also been used for clutter suppression, but they are limited by accuracy of the downmixing matrix and the low number of Doppler samples available in focused transmission scheme (Yu, Johnston, & Cobbold, 2007). Wavelet transform based filters based on an amplitude thresholding method to reject high energy wavelet coefficients corresponding to clutter can falsely diminish bright objects that are not artifacts in the ultrasound image (C. Tay, Acton, & Hossack, 2011). Moreover, there is no regular rule for the wavelet base selection, it commonly depends on the users' experience. Since the threshold value used to separate clutter from blood depends on the selected wavelet, the filtering performance of the wavelet transform based methods may vary. Empirical Mode Decomposition (EMD) method has also been used for clutter filtering. The problem however with EMD based filter is that it decomposes the signal residue at each stage by using a sifting procedure, which is nonlinear and can cause phase distortion resulting in poor clutter and blood separation (Zhang, Gao, Wang, Chen, & Shi, 2007).

1.2.7 Eigen-based Clutter Filtering: Advantages and Limitations

The emergence of eigen based clutter filtering has helped overcome the limitations of conventional clutter filtering methods by using both spatial and temporal information to better distinguish between tissue clutter and blood subspace (Yu & Lovstakken, 2010), (You & Wang, Oct 2009), (Song, Zhang, & Gong, Dec 2006). Eigen based filtering has strongly benefited from the long Doppler ensembles obtainable by HFR plane wave imaging (Bayat & Fatemi, 2018). Singular value decomposition (SVD) of raw ultrasonic data generates singular values whose amplitude decay allows removal of the high energy clutter components (Song, Manduca, Trzasko, & Chen, 2016). Singular vectors produced by SVD contain spatiotemporal information that can be used to identify and reject tissue clutter from the blood flow signal (Demené, et al., 2015). Attempts to overcome the high computational cost associated with SVD filtering of large data volumes have also been reported (Song, et al., 2017), (Chee, Yiu, & Yu, 2017).

Although SVD based filtering has established itself as a good method for clutter rejection, there is however no standard approach yet to determine the eigen components belonging to tissue clutter. Several SVD based filtering methods have been reported to achieve clutter rank selection. Each of these techniques have their own limitations. Kruse and Ferrara presented a fixed eigen rank threshold for clutter based on the amplitude of eigenvalues (Kruse & Ferrara, 2002). Yu and Cobbold proposed a Hankel-SVD filter formulation which uses mean frequency of singular vectors to select the clutter rank (Yu & Cobbold, 2008). Arnal *et al.* formed a spatial similarity matrix (SSM) from singular vectors to find the singular value threshold that separates the tissue and blood subspace (Arnal, Baranger, Demene, Tanter, & Pernot, 2017). Filtering performance of all these clutter rank estimation strategies depends highly on the quality of the involved data statistics. For e.g., computing the correct eigen rank threshold for clutter based on the singular value amplitude can become difficult for larger ensemble sizes. Moreover, in the SSM method identifying the tissue and blood spatial correlation squares is not

always possible since blood correlation can rather represent an elliptic shape (Baranger, et al., 2018). A hand-tuned cut-off frequency needs to be defined for the Hankel-SVD filter and it can lose performance when blood and tissue frequencies overlap.

1.2.8 Data Clustering in Biomedical Imaging

Clustering is an unsupervised machine learning tool for grouping data points which is commonly used in several fields, including image segmentation, bioinformatics, data mining etc. Many clustering methods have been reported in literature for biomedical image segmentation. For e.g., Wu *et al.* used color-based K-means clustering for brain tumor detection (Wu, Lin, & Chang, 2007). Beevi *et al.* used fuzzy c-means clustering for MRI image segmentation (Beevi, Sathik, & Senthamaraikannan, 2010). Moubark *et al.* used K-means clustering for classification and removal of tissue clutter from ultrasound image based on an energy criterion (Moubark, Harput, Cowell, & Freear, 2016).

1.3 Outline of Thesis Study

1.3.1 Motivation and Hypothesis

Blood flow detection in ultrasound imaging is a challenging task in certain clinical scenarios e.g., slow-flow detection and assessing blood flow with fast tissue motion. Clutter arising from tissue motion has much stronger energy than blood. Hence, unsuppressed tissue clutter significantly hampers blood flow visualization and biases velocity estimation (Bjaerum, Torp, & Kristoffersen, 2002). Furthermore, flow detection performance suffers if tissue and flow signal subspaces overlap after eigen components are projected to a linear feature space for clutter rank selection. Instead of relying on just one specific feature, the rich information present in the unfocused plane wave transmission dataset can potentially be further utilized for clutter removal. The guiding hypothesis is that since tissue clutter and blood signals have different spatiotemporal and energy characteristics, a clustering algorithm can

exploit these distinctive properties to adaptively identify and suppress eigen components corresponding to clutter, and in turn improve blood flow detection performance.

1.3.2 Research Objectives

The overall goal of this project is to enhance flow detection performance by developing a robust clutter rank estimation technique which uses the spatiotemporal and energy information available in the data to detect and reject tissue clutter effectively. Specifically, this work will seek to achieve the following three research objectives:

1) Develop a novel multivariate clustering based clutter rank estimator that is fully automated (independent of tissue/blood threshold hand tuning) and adaptively detects and removes non-blood eigen components by considering multiple signal features extracted using SVD.

2) Evaluate the flow detection performance of the proposed method *in vitro* through a flow phantom testbed design which exhibits acoustic properties similar to human arteries and soft tissue.

3) Assess the flow detection performance of the proposed method *in vivo*, where the data characteristics are most realistic.

4) Quantitatively compare the statistical flow detection performance of the proposed method with the current clutter rank estimation methods using receiver operating characteristic (ROC) analyses.

Chapter 2 Robust Eigen-filter Design for Ultrasound Flow Imaging

2.1 Chapter Overview

This chapter explains in detail the design of the proposed multivariate clustering based SVD filter. Section 2.2 first gives an overview of the eigen-filtering framework, starting with the fundamentals of the Ultrasound Doppler signal components. Next, the basics of SVD are introduced, followed by an explanation of how multiple image features are generated from the decomposed components to aid in discrimination between clutter and blood signal. Furthermore, K-means clustering for clutter rank estimation was introduced and the eigen-image analysis was specified to establish ground truth reference for clutter and blood rank estimation. The last section outlined the procedure for ROC analysis to determine the comparative flow detection performance of the proposed method with other clutter rank estimation techniques.

2.2 Methodology

The theoretical design behind multivariate clustering based eigen-filter is explained stepwise in this chapter. Fig. 2.1 illustrates all the methods in steps corresponding to the proposed eigen-filtering framework reported earlier in (Waraich, Chee, Xiao, Yiu, & Yu, 2019). The raw data ensemble is first reshaped to a 2-D space-time Casorati matrix which then undergoes SVD to yield the singular values and the left/right singular vectors. Multiple signal features are then extracted from these three decomposed matrices to aid in the discrimination of tissue clutter, blood and noise signals. The three matrices are then supplemented for clustering which groups eigen components into tissue clutter, blood & noise clusters. Eigen components corresponding to the non-blood clusters are removed and post-filtered power Doppler maps overlaid on B-mode image are created from the reconstructed images.

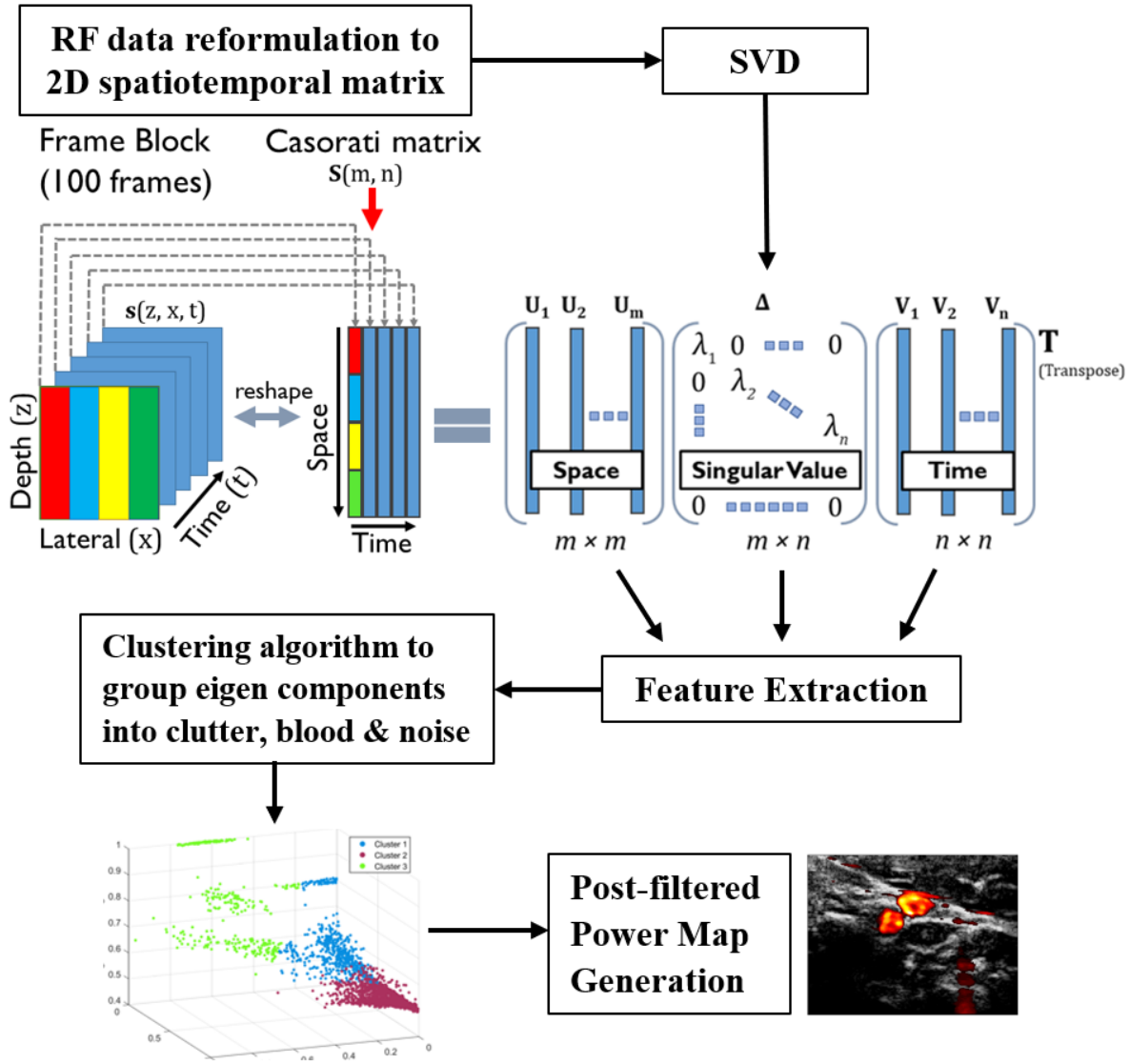

Fig. 2.1. Overview of the multivariate clustering based eigen-filtering framework. The raw data ensemble (frame block) *s(x, z, t)* has a slow-time dimension *t* and two spatial dimensions including *x* (lateral) and *z* (depth). The frame block is reshaped to a 2-D space-time Casorati matrix *S* by stacking columns within a frame into a single column in *S* and repeating this procedure for all slow-time frames. SVD is next performed on *S* to yield the diagonal matrix and the left/right singular vectors. Multiple signal features are generated from the three decomposed matrices which are then supplemented for clustering. The clustering algorithm groups eigen components into clutter, blood & noise clusters. Eigen values corresponding to the non-blood clusters are removed and post-filtered power Doppler maps overlaid on B-mode background are generated from the reconstructed images.

2.2.1 Ultrasound Doppler Signal Components

The US Doppler flow signal is represented as the summation of three components: tissue clutter, blood and electronic/ thermal noise. A typical beamformed ultrasound RF data matrix is described as a cineloop of 2-D images. Mathematically, the raw data matrix is a three-dimensional (3-D) complex variable $s(x, z, t)$ of size (N_z , N_x , N_t), where one dimension is time t and the other two are spatial dimensions x (lateral) and z (depth).

2.2.2 Singular Value Decomposition

The raw data ensemble $s(x, z, t)$ is reshaped to a spatiotemporal Casorati matrix (Candès, Sing-Long, & Trzasko, 2013) which rearranges the data into a 2-D space-time matrix $\boldsymbol{S}$ of size $(N_z \times N_x , N_t)$. SVD is performed on the Casorati matrix $\boldsymbol{S}$ which yields the product of the following three matrices:

$$\boldsymbol{S} = \boldsymbol{UDV}^* \tag{2-1}$$

Where matrices **U** and **V** are unitary matrices with dimensions $(N_z \times N_x, N_z \times N_x)$ and (N_t , N_t) respectively. * stands for the conjugate transpose and **D** is a diagonal matrix of size $(N_z \times N_x, N_t)$ with diagonal values λ_k sorted in a descending energy order. $\boldsymbol{S}$ is decomposed into eigen-components λ_k and each component consists of **U** and **V** vectors scaled by **D**. The rows of matrix $\boldsymbol{S}$ contain the raw spatial information, while its columns represent the time dimension. Thus, the SVD of $\boldsymbol{S}$ results in the singular vectors of **U** that provide spatial information while singular vectors of **V** represent the temporal information in $\boldsymbol{S}$.

2.2.3 Generation of Image Statistics

The following three signal features were extracted from the singular values and left/right singular vectors to aid in discrimination between tissue clutter and blood signals.

Singular Value Magnitude

Clutter from tissue structures is generally much more echogenic than the blood signal due to its relatively high acoustic impedance mismatch (Bjaerum, Torp, & Kristoffersen, 2002). This difference in power between tissue clutter and the blood signals can be seen in the singular value magnitude decay curve as shown in Fig. 2.2(a).

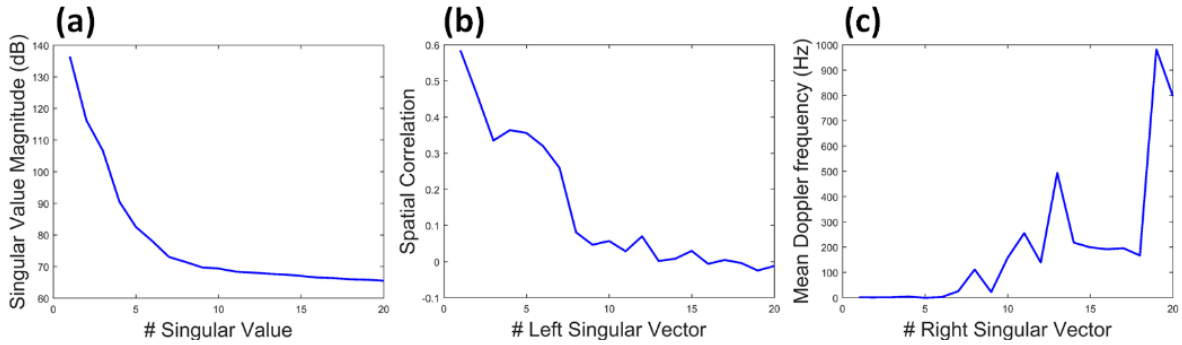

Fig. 2.2. (a) Singular values λ_k of matrix D expressed in dB, (b) Spatial correlation curve (correlation of the first singular vector U_1 with left singular vectors $|U_k|$ $k \in [1, N_t]$), (c) Mean Doppler frequency estimation curve of the right singular vectors, for a plane wave HFR Doppler acquisition on an *in vivo* carotid region.

Spatial Correlation

In US imaging, it has been widely reported that tissue clutter has a much higher spatial coherence relative to blood since it is far less deformable then the blood scatterers which have low viscosity compared to tissue (Demené, et al., 2015). Fig. 2.3 illustrates the spatial difference between clutter and blood eigen images which can be leveraged by computing the spatial correlation between the first spatial singular vector $\mathbf{U_1}$ (typically representative of tissue clutter) and the spatial singular vectors $|\mathbf{U_k}|$ $\boldsymbol{k} \in [1, N_t]$.

$$C = \frac{1}{N_x \cdot N_z} \sum_{k=1}^{N_t} \frac{(|U_1| - \overline{|U_1|}) \cdot (|U_k| - \overline{|U_k|})}{\sigma_1 \cdot \sigma_k} \tag{2-2}$$

Where $\overline{\mathbf{U_k}}$ stands for the mean and $\boldsymbol{\sigma_k}$ is the standard deviation of $\mathbf{U_k}$ indexes**.** N_x and N_z are the lateral and depth dimension size respectively of the original raw data matrix *s*. **C** is the spatial correlation vector of size (1, N_t) which reveals high spatial correlation for low-order singular vectors corresponding to tissue clutter and low spatial correlation in high-order singular vectors typically corresponding to blood and noise as shown in Fig. 2.2(b).

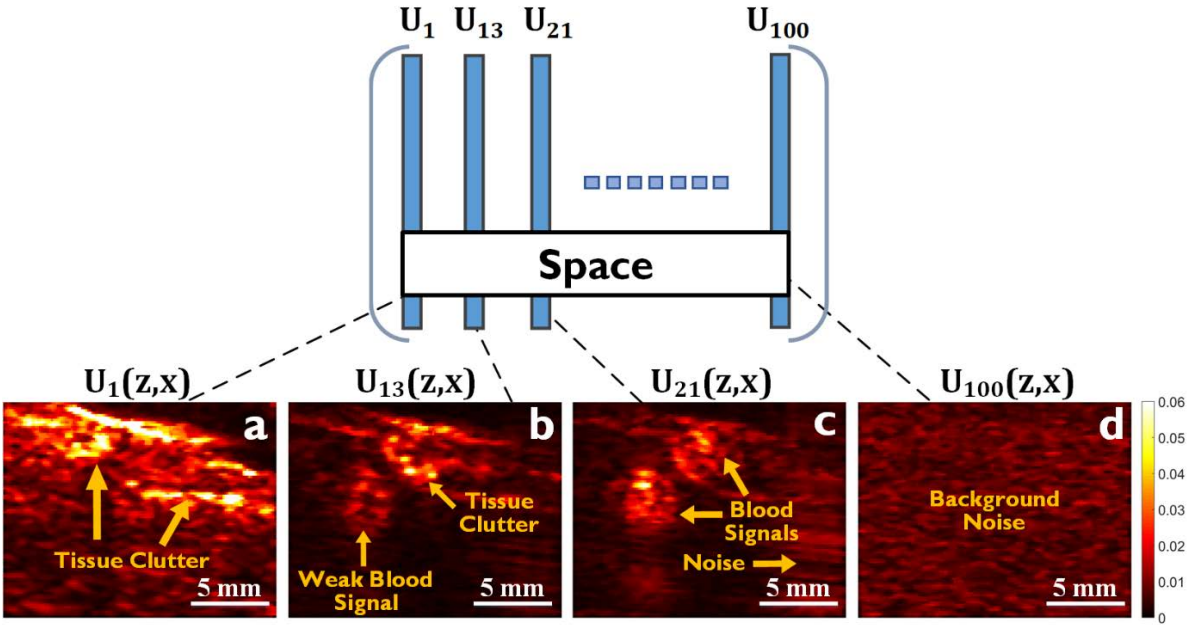

Fig. 2.3. Illustration of spatial eigen images generated from left singular vectors by reshaping them back to raw image dimensions. (a) U_1 shows the strong clutter originating from the vessel wall and surrounding tissue. (b) U_{13} demonstrates the overlap between vessel wall clutter and weak blood signal. (c) U_{21} shows the strong blood signals in vessel lumens along with background noise. (d) U_{100} just shows background noise signal.

Mean Doppler Frequency

Tissue clutter being relatively slower than blood, dominates the low temporal frequencies whereas blood echoes exhibit high frequency motion (Bjaerum, Torp, & Kristoffersen, 2002). Fig. 2.4 shows the temporal difference between the clutter and blood signals that can be used by calculating the mean Doppler frequency for each temporal (right) singular vector $\mathbf{V_k}$ using the following lag-one autocorrelation based estimator:

$$\widehat{R}_k = \sum_{i=1}^{N_t-1} V_k^*(i) \cdot V_k(i+1) \tag{2-3}$$

$$\hat{f}_k = \frac{PRF}{2\pi} \times arctan\left(\frac{imag(\widehat{R}_k)}{real(\widehat{R}_k)}\right) \tag{2-4}$$

Where $\hat{f}_k$ is the mean Doppler frequency estimate for the k[th] singular vector $\mathbf{V_k}$. * stands for the conjugate transpose. Mean Doppler frequency estimation curve of the right singular vectors is shown in Fig. 2.2(c).

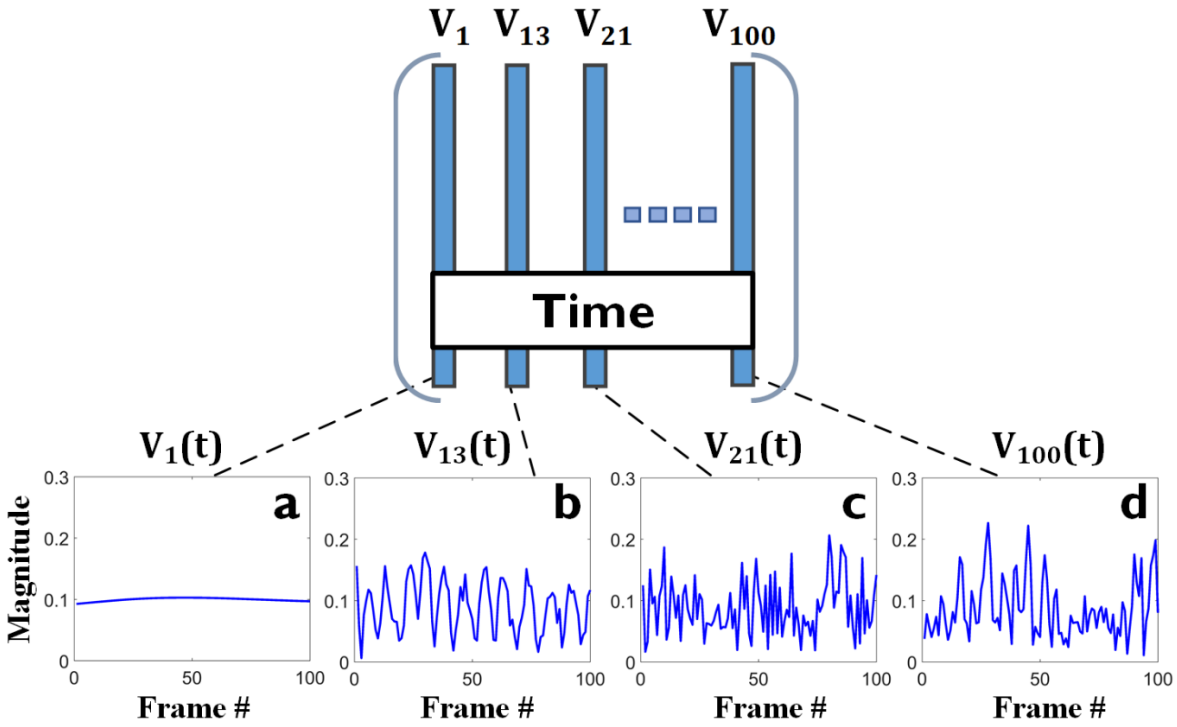

Fig. 2.4. Temporal criteria for mean Doppler frequency computation. (a) V_1 shows that tissue clutter has a near constant temporal magnitude. (b) V_{13} shows random temporal fluctuations corresponding to mixed clutter and weak blood signal. (c)-(d) Right singular vectors describe the strong random temporal fluctuations corresponding to blood and background noise signals.

2.2.4 K-means Clustering for Adaptive Clutter Filtering

There are three clusters of interest in the raw ultrasound data based on the Doppler flow signal components: clutter, blood and noise. Since the number of clusters are known in advance and the data

is unsupervised, K-means is preferred for clustering. Gaussian Mixture Model (GMM) based clustering was not used as the data violates the Gaussian assumption. Fuzzy clustering is not relevant to this application since each data point cannot be a part of more than one cluster. Density based clustering requires a distance threshold which can be difficult to set. K-means clustering (Lloyd's algorithm) (Lloyd, 1982) is applied on the three-dimensional data formed from the extracted image statistics. Each of the three statistics were computed from the SVD of five consecutive frame blocks, where each frame block contains a sequence of 100 frames. Cluster centroids were initialized using the K-means++ algorithm (Arthur & Vassilvitskii, 2007). K-means iteratively calculates the squared Euclidean distance between the data points and cluster centroids to allocate each point to the closest cluster. The centroids are recomputed in each iteration by evaluating the mean of all points in that centroid's cluster until the centroid positions do not change and the algorithm converges to an optimal result. Number of clusters were pre-defined as three, where each cluster represents one of tissue, blood and noise component. The cluster with the highest mean singular value magnitude and spatial correlation and the lowest mean Doppler frequency is classified as tissue clutter. The cluster with the highest mean Doppler frequency is classified as noise.

2.2.5 Suppression of Tissue Clutter and Noise Components

Each cluster contains separate data points from the total five consecutive frame blocks (5×100 frames). The eigen components corresponding to the tissue and noise clusters are then set to zero for suppression of clutter and noise data points belonging to each of the five frame blocks.

2.2.6 Power Doppler (PD) Flow Map Construction

Equation (2-1) is used to perform reverse SVD where the diagonal matrix *D* contained the filtered singular values. Post-filtered image matrix is then constructed by reshaping the matrix $\boldsymbol{S}$ from (2-1) back to the raw data ensemble $s(x, z, t)$ dimensions. The power estimates are generated by computing

the mean-squared sum of the filtered data ensemble using (2-5). The power estimates are log compressed when displaying the PD image.

$$\boldsymbol{PD(x,z) = \int_{i=1}^{N_t} |s(x,z,t)|^2 dt} \tag{2-5}$$

2.2.7 Eigen-image Analysis

Spatial eigen-images were generated from left singular vectors by reshaping them back to image dimensions of the raw data matrix *s*. These eigen-images served as ground truth reference for showing the clutter, blood or noise signal contributions in each left singular vector. For each left singular vector's spatial eigen image, the blood-to-clutter (BCR) ratio was computed using the following:

$$\boldsymbol{BCR = 20log_{10}\left(\frac{M_{flow}}{M_{tissue}}\right)} \tag{2-6}$$

Where M_{flow} is the mean Doppler power of the flow pixels in both carotid and vein flow regions, while M_{tissue} is the mean Doppler power of the tissue pixels outside the flow regions.

2.3 ROC Analysis for Flow Detection Performance Investigation

2.3.1 Comparison with Different Clutter Rank Estimation Methods

To obtain data for comparison, clutter filtering was also performed using the following eigen-based clutter rank estimators:

1. A frequency filter based on fixed cut-off frequencies that are hand tuned for both clutter and noise removal (Baranger, et al., 2018).
2. A spatial coherence filter which involves the spatial similarity matrix (SSM) based clutter and noise suppression method (Baranger, et al., 2018).

3. A magnitude filter whose clutter threshold is based on the turning point of the singular value curve (Baranger, et al., 2018).

All these filters operated on a slow-time ensemble size of 100 frames. Post-filtered power Doppler maps corresponding to each method were obtained for ROC analysis.

2.3.2 Tissue and Flow Region Identification

The boundaries between blood flow and tissue region were demarcated on the cross-sectional grayscale B-mode image of the PVA-based straight tube (see Fig. 2.5(a)) and the carotid and vein region (see Fig. 2.5(b)) for ROC analysis. MATLAB's built-in contour tool was used for selecting the regions of interest. Fig. 2.5(a) shows the vessel lumen flow region (blue dashed circle) selected as the hypoechoic B-mode pixels inside the vessel walls, while the tissue region are all the B-mode pixels surrounding the flow region. Similarly, Fig. 2.5(b) shows the carotid flow region (red dashed circle) and jugular vein flow region (blue dashed circle) is selected as the hypoechoic B-mode pixels inside the vessel walls, while the tissue region are all the B-mode pixels outside the flow region.

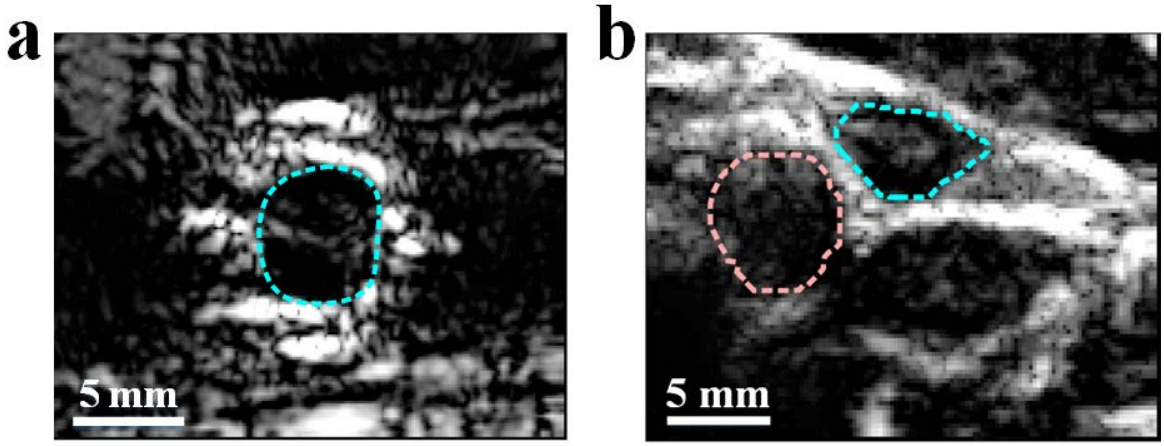

Fig. 2.5. Ultrasound B-mode images showing (a) short-axis view of the PVA-based straight tube with the vessel lumen flow region highlighted with blue dashed circle. (b) cross-sectional view of the *in vivo* Common Carotid Artery (CCA) flow region (red dashed circle) and Jugular Vein (JV) flow region (blue dashed circle).

2.3.3 Generation of ROC Curves

Pixel values corresponding to the identified tissue and flow regions were extracted from the post-filtered power Doppler maps of each clutter rank estimation technique. Two statistical parameters were then computed for different power Doppler thresholds (swept in 0.2 dB increments from 0 to 100 dB): true positive rate (TPR) and the false alarm rate (FAR). The TPR or sensitivity was defined as the percentage of flow pixels with post-filtered Doppler power higher than the threshold value, while the FAR (1-Specificity) was defined as the percentage of tissue pixels with post-filtered Doppler power higher than the threshold value. The ROC curves for each filter were plotted with their respective TPR against the corresponding FAR. The area under the ROC curve (AUC) quantifies the diagnostic performance in ROC analysis. The higher the AUC value is the better the detection performance (Zweig & Campbell, 1993). The AUC was also computed to quantitatively evaluate how well each clutter rank estimator was able to distinguish between the tissue and flow region.

2.4 Chapter Summary

This chapter explained in detail the theoretical framework behind multivariate clustering based eigen-filter. The ultrasound Doppler signal is first converted into a 2-D space-time Casorati matrix formulation which after undergoing SVD, produced left singular vectors which encode the spatial information and right singular vectors that contained the time information. Next, three key spatiotemporal image features (singular value magnitude, spatial correlation and mean frequency) were generated from the singular values and left/right singular vectors to aid in discrimination between tissue clutter and blood signals. The K-means clustering algorithm was applied on the 3-D distribution of image features to group data points into clutter, blood & noise clusters. Eigen values corresponding to the non-blood clusters were removed and post-filtered power Doppler maps overlaid on B-mode background were generated from the reconstructed images. As part of eigen-image analysis, spatial

eigen-images were produced and BCR was calculated for each eigen-image to serve as ground truth reference for showing the clutter, blood or noise signal contributions in each left singular vector. To statistically evaluate the flow detection performance of the proposed filter in comparison with other clutter rank estimators, ROC analysis procedure was defined in detail.

Chapter 3 *In Vitro* and *In Vivo* Experimental Setup

3.1 Chapter Overview

This chapter describes the *in vitro* and *in vivo* experimental methods used to test the proposed K-means based SVD filters' flow detection performance. Section 3.2 outlines the complete flow phantom testbed design, which includes 3D printing of a phantom box, fabrication of a compliant vessel tube and tissue mimicking slab. Next, details about blood mimicking fluid formation is given which is pumped through the flow phantom using an in-house programmable flow pump system. This section also describes the development of a vibratory stage which is used to synthesize tissue clutter. Section 3.3 introduces the high-frame-rate data acquisition parameters and imaging hardware used for both the flow phantom and *in vivo* experiment. Section 3.4 explains the receive beamforming method and lists the ultrasound image formation parameters.

3.2 Flow Phantom Testbed Design

Fig. 3.1 below shows the complete flow phantom testbed design to evaluate comparative flow detection performance of the K-means based SVD filter with other clutter rank estimation methods. This testbed is composed of three important components:

1) A compliant straight tube vessel whose wall elasticity mimics human arteries.
2) A vibratory stage that synthesizes tissue vibrations which resemble motion from extrinsic sources such as operator hand tremor.
3) A flow pump system that produces pulsatile flow similar to heart circulation.

Comprehensive description of each component of this testbed is given below.

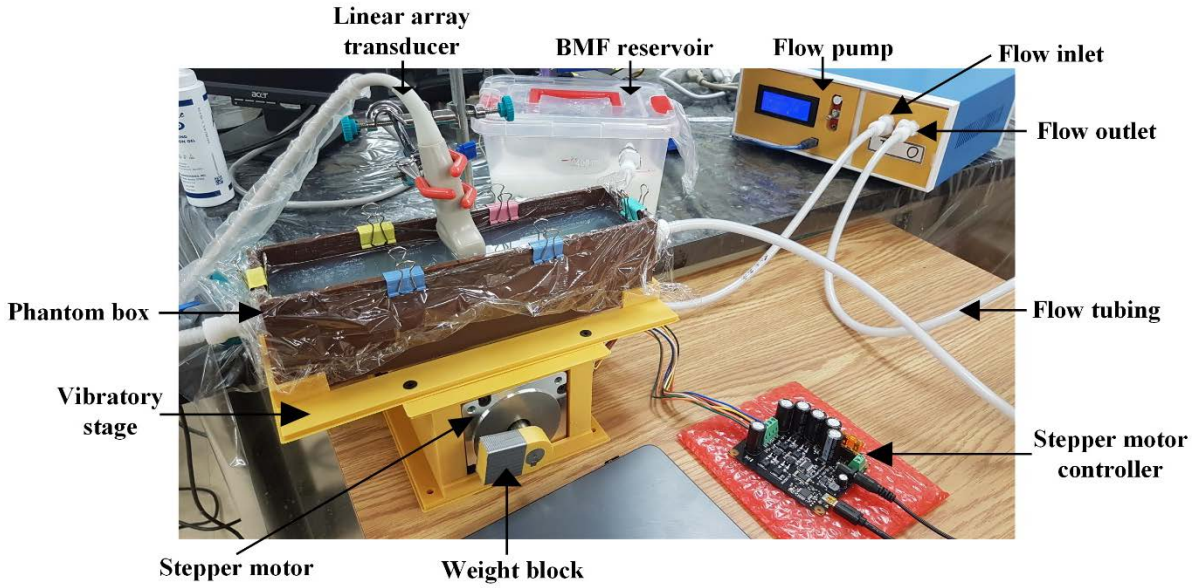

Fig. 3.1. Overview of the flow phantom testbed design showing the flow phantom box placed on top of the vibratory stage. The phantom box contains the compliant straight tube vessel inside, immersed in a tissue mimicking slab. The phantom box is connected in a closed circuit loop to the flow pump system and the blood-mimicking fluid (BMF) reservoir using flow tubing to receive pulsatile flow. The linear array transducer is placed on top of the flow phantom through a metal stand support to image in short-axis view.

3.2.1 Fabrication of Phantom Box

The flow phantom design framework began with CAD modelling of the phantom box shown in Fig. 3.1. Its geometry was designed on SolidWorks (Dassault Systèmes, Waltham, MA, USA). The box was constructed as a solid cuboid containing a volumetric cavity for placing the vessel tube. With an inner dimension of 293×77×71 mm^3 (length×width×height), the CAD model was exported as a stereolithography (STL) file that defines the geometry of the phantom box. The STL file was then sent for 3-D printing via a fused deposition modeling (FDM) system (model DX; Creatbot 3D Printer, Zhengzhou, China). For this 3-D printing process, the printer resolution in the vertical direction is determined by the layer thickness parameter which was set to 0.1 mm. The printer resolution in the horizontal direction is determined by the extruder head size, which was set to 0.25 mm. The print material used was Polylactic acid (PLA).

3.2.2 Fabrication of PVA-based Vessel Tube

The geometry of the straight tube vessel was modelled using SolidWorks. The vessel tube had a length of 180 mm, with an inner diameter of 6 mm and wall thickness of 1.5 mm. It was developed physically using an investment casting protocol previously reported (Dineley, Meagher, Poepping, Dicken, & Hoskins, 2006). The material composition of the vessel wall is given in Table 3.1 below. The elasticity of the vessel wall was set by administering three freeze–thaw cycles that alternated between −20 °C and 4 °C for 24 hours each to crystalize the PVA molecules. The fabricated PVA-based vessel tube [see Fig. 3.2] was mounted onto flow connectors (EW-06361-61; Cole-Parmer, Vernon Hills, IL, USA) attached to the two ends of the phantom box. The PVA-based vessel tube had an elastic modulus of 106.1 kPa as measured using a tensile micro tester. Table 3.2 further lists the experimentally derived acoustic properties of the PVA-based vessel tube in comparison with human soft tissue (Chee, Ho, Yiu, & Yu, 2016).

Table 3.1. PVA-based vessel tube fabrication.

Percentage (by weight)	**Material**	**Part number and Manufacturer**
10%	Polyvinyl alcohol (PVA)	341584; Sigma-Aldrich
3%	Fine graphite powder	282863; Sigma-Aldrich
0.3%	Potassium sorbate	85520; Sigma-Aldrich

Table 3.2. Acoustic properties of PVA-based vessel tube and human soft tissue.

Parameters	**PVA-based Vessel Tube**	**Human tissue**
Attenuation coefficient (dB/cm·MHz)	0.229 ± 0.032	0.3-0.7
Acoustic speed (m/s)	1535 ± 2.4	1540

Fig. 3.2. Picture of the PVA-based straight tube vessel before mounting it in the phantom box.

3.2.3 Tissue Mimicking Material Formation

A tissue mimicking slab was prepared for the flow phantom using an agar-gelatin mixture. The chemical composition of the mixture is shown in Table 3.2 below. The mixture was prepared at 90 °C in solution form and then machine stirred until the temperature of the agar-gelatin solution dropped to 45°C. Once cooled, it was poured into the phantom box cavity containing the PVA-based vessel tube and then refrigerated at 4 °C to form a slab around the vessel tube [see Fig. 3.3]. The phantom box was kept refrigerated prior to use in imaging experiment. The tissue slab had a measured acoustic speed of

1510 m/s (close to 1540 m/s in soft body tissues), an attenuation coefficient of 0.145 dB/(cm·MHz) and an elastic modulus of 35.9 kPa (Pinter & Lacefield, 2010).

Table 3.3. Agar-gelatin based tissue mimicking slab fabrication.

Percentage (by weight)	**Material**	**Part number and Manufacturer**
94.45%	Distilled water	N/A
1.5%	Agar	A1296; Sigma-Aldrich
3.75%	Gelatin	G2500; Sigma-Aldrich
0.3%	Potassium sorbate	85520; Sigma-Aldrich

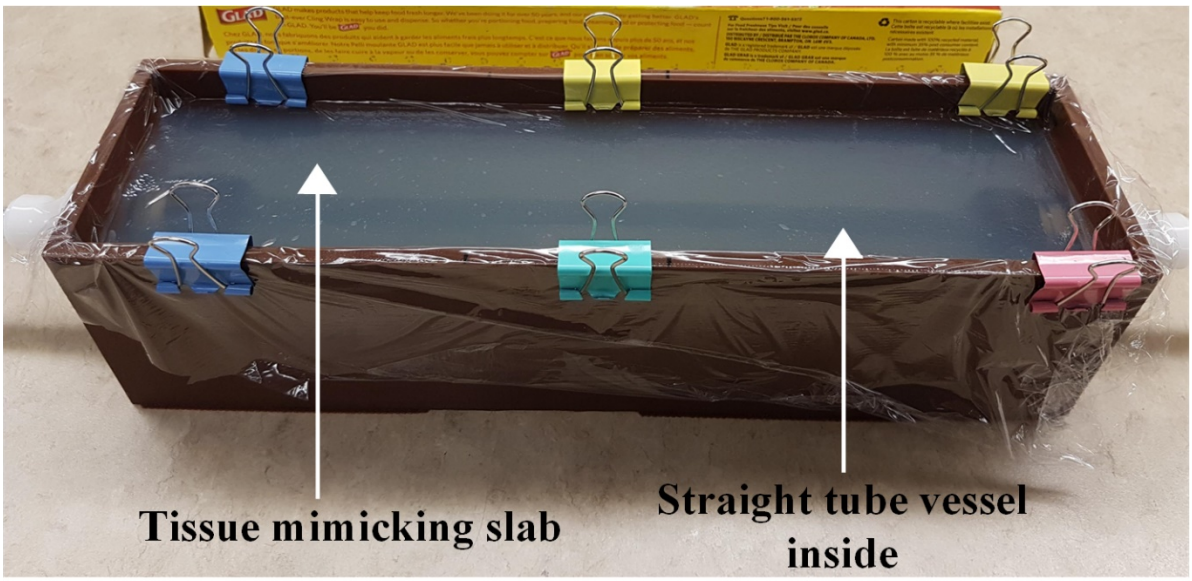

Fig. 3.3. Tissue mimicking slab formed in the phantom box after refrigeration. The PVA-based straight tube vessel can also be seen immersed in the tissue slab. A clear plastic wrap is used to cover the tissue slab to avoid formation of air bubbles in the slab.

3.2.4 Blood Mimicking Fluid Formation

A standardized protocol was used to make blood-mimicking fluid (BMF) (Ramnarine, Nassiri, Hoskins, & Lubbers, 1998) that had viscosity and acoustic scattering properties which match human blood. The detailed fabrication process has been reported previously by my lab (Ho, et al., 2017). Table 3.4 lists the ingredients required for its fabrication.

Table 3.4. Blood mimicking fluid formulation.

Percentage (by weight)	**Material**	**Part number and Manufacturer**
83.7%	Distilled water	N/A
1.8%	Organsol	2001 UD NAT1; Arkema
0.9%	Tergitol	86453; Sigma-Aldrich
10%	Glycerol	15514-029; Thermo Fisher Scientific
3.3%	Dextran	D4876; Sigma-Aldrich
0.3%	Potassium sorbate	85520; Sigma-Aldrich

3.2.5 Development of Vibratory Stage to Synthesize Tissue Motion

A vibratory stage was developed for tissue motion generation similar to the one previously reported from my lab (Chee & Yu, 2017). This stage synthesized slow-time clutter equivalent to extrinsic motion sources such as hand tremor of the ultrasound probe operator (Heimdal & Torp, 1997), (Tierney, Coolbaugh, Towse, & Byram, 2017). As shown in Fig. 3.1, the flow phantom box is placed over the vibratory stage which contains the following components:

1) A bipolar gearless stepper motor (86STH156 NEMA-34; Phidgets Inc., Calgary, Canada).

2) A bipolar stepper motor controller (1067_0B; Phidgets Inc., Calgary, Canada).

3) A 38-g weight block.

The stage housing the stepper motor was entirely modelled on SolidWorks [see Fig. 3.4] and printed using the 3D printer with PLA material. The stepper motor was first placed in the printed stage base and then the platform printed to hold the phantom box was screwed on top of the stage base. To build the vibrator, the weight block was attached to the stepper motor's shaft to induce an imbalanced torque that generates vibrations once the motor revolves. Next, the stepper motor was connected to the motor controller in a parallel wiring configuration to provide better torque at higher speeds. The stepper motor is rated to generate 122 kg-cm of holding torque at 4.2 Amps.

To spin the stepper motor, the motor controller was connected to a windows machine by USB cable and the automatically installed 'Phidget Control Panel' (INC, 2019) was used to adjust the motor's speed and acceleration. A digital photo laser tachometer (tach-mtr-01; CyberTech) was used to determine the speed of motor operation. In this work, the stepper motor was rotated at 900 r/min, which corresponds to a vibrational frequency of 15-Hz due to the imbalanced torque imposed on the motor. The motor's vibrational frequency induced physical motion in the phantom box in accordance with tissue vibration frequencies reported *in vivo* (Heimdal & Torp, 1997).

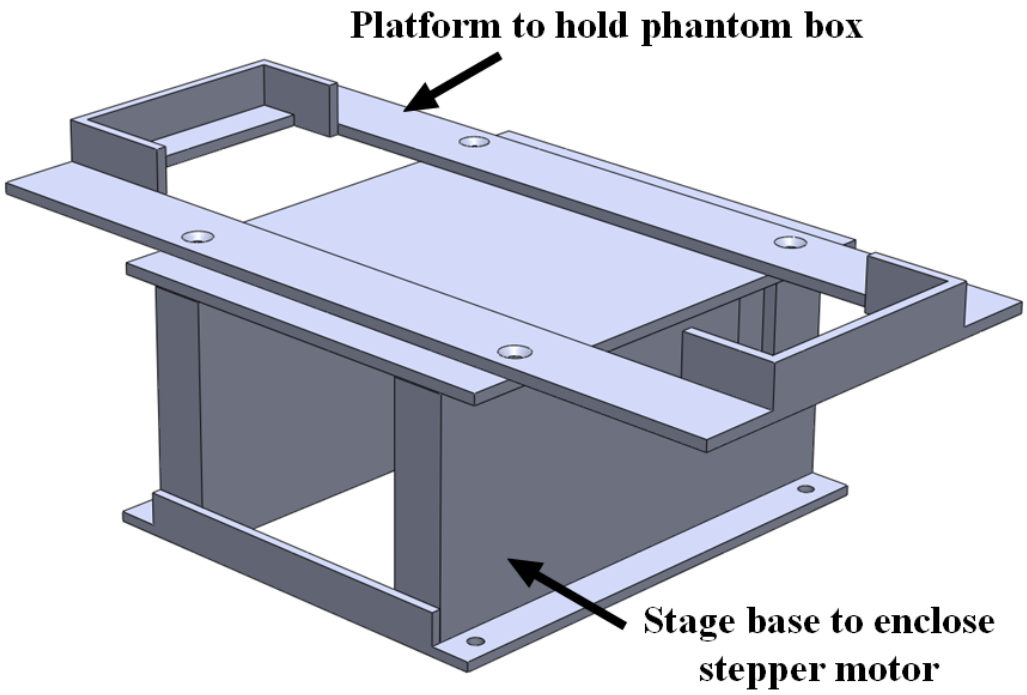

Fig. 3.4. Illustration of the vibratory stage CAD model showing the stage base that encloses the stepper motor and the platform to hold the phantom box which gets screwed on top of the stage base.

3.2.6 In-house Programmable Flow Pump

Overview of the Flow Pump System

An in-house flow pump system previously reported from my lab (Ho, et al., 2017) was used for the flow phantom experiment. This pump system allows the pulse shape and the flow rate to be modified as desired. The system itself consists of a servo motor that drives the gear pump, and an Arduino board to set the motor speed through the motor driver. For every pulse transmitted by the Arduino, the pump rotated by 0.001 of a revolution. Blood-mimicking fluid enters the gear pump from the BMF reservoir connected to the flow inlet of the pump. The user can set the waveform and flow rate desired by a knob connected to the Arduino and view the settings through an LCD panel also connected with the Arduino board.

Flow Circuit Setup

The pump system was connected to the flow phantom box placed on top of the vibratory stage. Using vinyl flow tubing the outlet of the flow pump system was connected to the inlet of the phantom box at one end. The outlet at the other end of the phantom box was connected to the inlet of the BMF reservoir. The flow circuit loop is completed by connecting the outlet of the BMF reservoir to the inlet of the flow pump system as shown in Fig. 3.1. Once this flow circuit was assembled, the flow pump system was configured to generate a carotid pulse (pulsatile flow profile) with a pulse rate of 60 beats/min and a peak systolic flow rate of 10 mL/s. The pulsatile flow profile from the pump system contained various key features similar to the human carotid flow waveform as shown in Fig. 3.5 below:

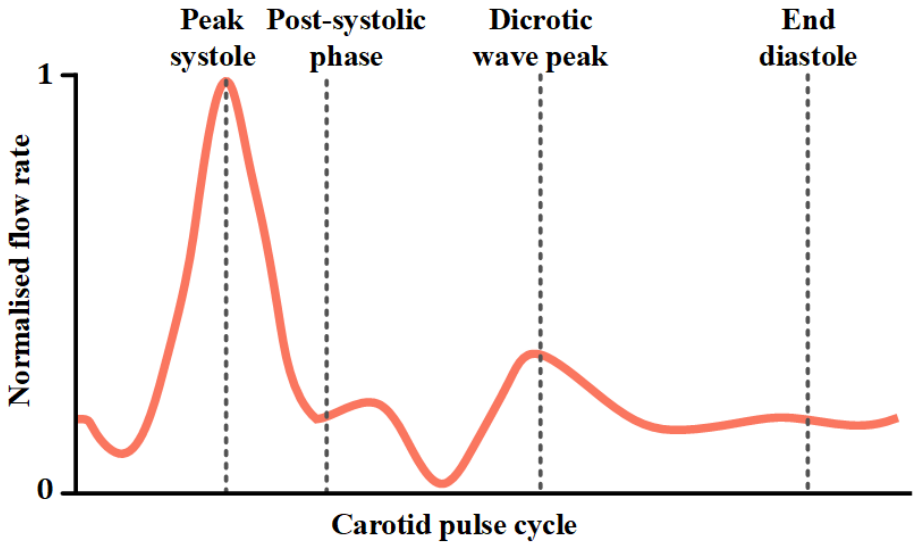

Fig. 3.5. Four essential phases of the human carotid flow waveform indicated by dashed lines corresponding to peak systole, post-systolic phase, dicrotic peak, and end diastole.

3.3 High-frame-rate Data Acquisition

3.3.1 Imaging Hardware for Flow Phantom Experiment

In vitro data acquisition for flow phantom experiment was done using a channel domain based imaging research platform in my lab. The imaging platform is composed of the following parts: 1) a customizable front-end core (SonixTouch; Analogic Ultrasound, Peabody, MA, USA) which allows transmission and reception programming of each array element, (2) a multi-channel pre-beamformed data acquisition tool. The data acquired was streamed to a back-end computer that processes data further using a GPU (So, Chen, Yiu, & Yu, 2011). For ultrasound transmission and reception, a 128-element linear array (L14-5/38; Analogic Ultrasound) was used.

3.3.2 Data Acquisition for Flow Phantom Experiment

For the flow phantom experimentation, the linear array transducer configured for HFR plane wave imaging was aligned to scan along the short axis view of the flow phantom. The TEXO software development kit (Analogic Ultrasound) was used to program the transmit firing sequence to generate plane waves at three transmit-receive steering angle pairs (-10°, 0°, +10°) with a center frequency of 5 MHz. Remaining parameters used for data acquisition are listed in Table 3.5.

Table 3.5. Imaging parameters for flow phantom data acquisition.

Parameter	**Value**
Plane Wave Imaging	
Imaging Center Frequency	5 MHz
Pulse Repetition Frequency, f_{PRF}	10 kHz
Effective Data Acquisition Rate, f_{DAQ}	3.3 kHz
Sampling Frequency	40 MHz
# Transmit/Receive channels	128

Pulse Duration (# cycles)	3
Steering Angles	-10°, 0°, +10°
Data Acquisition Duration	1 sec
Image Formation Processing	
FIR Filter Pass Band	3 to 7 MHz
FIR Filter Taps	225
Stop-band Suppression	100 dB
Apodization	Hanning window

3.3.3 Imaging Hardware for *In Vivo* Investigation

In vivo data acquisition was done using a research purpose ultrasound scanning open-platform available in my laboratory (Yiu, Walczak, Lewandowski, & Yu, 2019). This platform contains three parts: 1) a front-end 192 channel ultrasound module; 2) a GPU processing unit (GTX 1080Ti; NVidia Corporation, Santa Clara, CA, USA); and 3) a back-end computer (TSB7053; Trenton Systems, Lawrenceville, GA, USA). All these parts are connected through a peripheral component interconnect express back-plane. A 192-element linear array transducer (SL1543; Esaote, Genova, Italy) probe was used for transmitting and receiving ultrasound pulse-echoes.

3.3.4 Data Acquisition for *In Vivo* Investigation

For *in vivo* investigation, a healthy male subject (age 28 years) volunteered to have ultrasound examination done for this study. The linear array probe configured for HFR plane wave imaging was placed on the subject's neck (3 cm from the carotid bulb), to image the common carotid artery (CCA) and jugular vein (JV) region in short-axis view. Extrinsic tissue motion was induced in the dataset by voluntary probe motion to test the efficacy of the clutter filtering methods. Raw plane wave data acquisition was performed at 5 MHz imaging frequency. HFR Doppler acquisition was done using a

steering angle of -10° and interleaved B-mode firings were done using 30 angles (ranging from -15 to 15 degrees (excluding 0°) with 1° incremental steps), resulting in an effective PRF of 3 kHz. Detailed imaging parameters for this experiment are listed in Table 3.6.

Table 3.6. Imaging parameters for *in vivo* data acquisition.

Parameter	**Value**
Plane Wave Imaging	
Imaging Center Frequency	5 MHz
Pulse Repetition Frequency, f_{PRF}	6 kHz
Effective Data Acquisition Rate, f_{DAQ}	3 kHz
Sampling Frequency	25 MHz
Transmit Aperture Size (# channels)	192
Pulse Duration (# cycles)	2
Doppler Steering Angle	-10°
B-mode Steering Angles	[-15° to 15° (excluding 0°); 1° increments]
Data Acquisition Duration	2.6 sec
Image Formation Processing	
FIR Filter Pass Band	4 to 8 MHz
FIR Filter Taps	64
Beamformer Aperture Size (# channels)	96
Apodization	Hanning window
Hilbert transform Filter Taps	51

3.4 Ultrasound Image Formation

3.4.1 Receive Beamforming

In general, once the RF data acquisition is complete, the data is transferred offline to the back-end processor. The pre-beamformed data is first filtered through a FIR filter with passband frequencies listed in Table 3.5 and 3.6 to increase the SNR. Hilbert transform is next applied to the filtered signal to yield the imaginary part of the analytic RF signal. The FIR filtered signal represents the real part of the analytic RF signal. Next, delay-and-sum beamforming method using GPUs reported earlier by my lab (Yiu, Tsang, & Yu, 2011) was applied on the complex signal. Mainly receive beamforming is achieved through calculation of the depth information by computing the two-way time of flight delays of the pulse-echoes received by each array element. Since multiple transmit-receive steering angles were used, the resultant low-resolution beamformed images were coherently compounded to form one high-resolution image.

3.4.2 Image Formation Parameters

The post-beamformed image parameters for both flow phantom imaging and *in vivo* imaging experiment are listed in detail in Table 3.7 and 3.8 below:

Table 3.7. Post-beamformed image parameters for flow phantom imaging.

Parameter	**Value**
Image Size (# pixels)	147 × 231
Axial Pixel Resolution (mm)	0.1
Lateral Pixel Resolution (mm)	0.1
# Pixels in Axial Dimension (N_x)	147
# Pixels in Lateral Dimension (N_z)	231
Slow-time ensemble size (N_t)	100
Casorati matrix size ($N_z \times N_x$, N_t)	33957 × 100

Table 3.8. Post-beamformed image parameters for *in vivo* imaging study.

Parameter	**Value**
Image Size (# pixels)	91 × 137
Axial Pixel Resolution (mm)	0.15
Lateral Pixel Resolution (mm)	0.15
# Pixels in Axial Dimension (N_x)	91
# Pixels in Lateral Dimension (N_z)	137
Slow-time ensemble size (N_t)	100
Casorati matrix size ($N_z \times N_x$, N_t)	12467 × 100

3.5 Chapter Summary

Regarding the *in vitro* imaging experiment, the vibratory stage was used to generate motion frequency of 15 Hz in the flow phantom which induced physical motion in the phantom box in accordance with tissue vibration frequencies observed *in vivo*. The flow phantom contained a PVA-based vessel tube and a tissue mimicking slab that matched acoustic properties of human arteries and soft tissue respectively. This flow phantom served to demonstrate the flow detection capability of the proposed method at both peak systole (maximum vessel wall motion) and end diastole (slowest flow) phases of the carotid waveform. Flow detection capability of the proposed method was also tested *in vivo* in the CCA and JV region, where the data characteristics are most realistic. HFR plane wave imaging method at 5 MHz imaging frequency was used for both flow phantom and *in vivo* experiment.

Chapter 4 Experimental Results

4.1 Chapter Overview

This chapter presents the results for both flow phantom and *in vivo* experiments. Section 4.2 first shows the result of K-means clustering and next reports the comparative power Doppler maps for the proposed K-means based SVD filter and other clutter rank estimation methods. It also presents the results for ROC analysis and eigen component selection done by the proposed method and other clutter rank estimation techniques. Section 4.3 reports the results for the *in vivo* experiment in a similar order to the first section. It first shows the result of K-means clustering and next reports the comparative power Doppler maps for the proposed K-means based SVD filter and other clutter rank estimation methods. It then presents comparative results of ROC analysis and eigen component selection for the proposed method and other clutter rank estimation techniques. In the end of this section, the effect of noise cluster suppression on flow detection is discussed.

4.2 Flow Phantom Experimental Results

4.2.1 Distinct Clusters Yielded by K-means Clustering

K-means clustered the data (convergence time: 8 ms) into discrete groups as shown in Fig. 4.1(a) below. Cluster 1 (blue) has the highest mean singular value magnitude and spatial correlation, and at the same time, the lowest mean Doppler frequency among all. These are typical properties of clutter originating from tissues and hence cluster 1 can be identified as tissue clutter. Cluster 3 (gray) has the least spatial correlation and the highest frequency content; both distinct features of noise. Upon identifying these two clusters, cluster 2 (red) can therefore be confidently attributed to signals from blood flow.

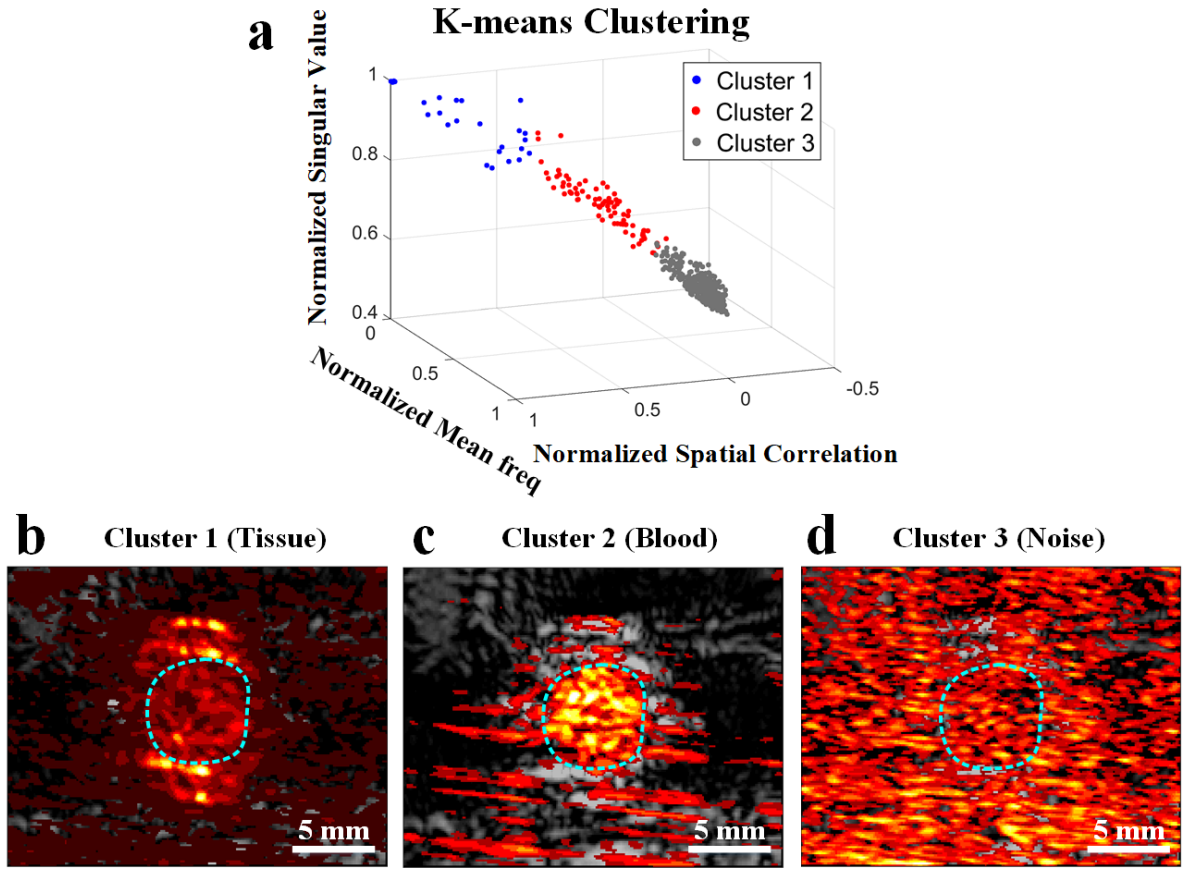

Fig. 4.1. (a) K-means clustering performed on the 3D distribution of image statistics acquired from the flow phantom at peak systolic phase of the cardiac cycle. (b)-(d) Representative spatial eigen-images from each cluster overlaid on B-mode image with lines demarcating the vessel lumen (blue dashed circle) flow region.

The group each cluster belongs to can also be qualitatively identified through its corresponding spatial eigen-image overlaid on B-mode image for reference. As expected, Fig. 4.1(b) shows the presence of strong vessel wall clutter in the eigen-image from cluster 1. It also shows presence of very weak blood signal in the vessel lumen flow region highlighted with a blue dashed circle. Since the vibrating tissue slab surrounding the vessel is also source of tissue clutter, it has also been identified as clutter by cluster 1. The spatial eigen-image in Fig. 4.1(c) clearly shows strong blood flow signal identified in the vessel lumen along with some weak surrounding noise signals by cluster 2. The spatial

eigen-image from cluster 3 is full of background noise as shown in Fig. 4.1(d).

4.2.2 K-means based SVD filter achieves Strong Flow Detection and Noise Suppression

K-means based clutter filtering strongly distinguished between flow and tissue regions at both end diastolic and peak systolic phase of the cardiac cycle in the presence of strong tissue motion caused by vessel wall pulsations and extrinsic tissue vibrations. Fig. 4.2 shows the post-filtered power Doppler maps at peak systole and end diastole corresponding to different clutter filtering methods which include the K-means based SVD filter [Fig. 4.2(a), (e)], frequency filter [Fig. 4.2(b), (f)], spatial coherence filter [Fig. 4.2(c), (g)], and magnitude filter [Fig. 4.2(d), (h)]. All power maps are rendered with a fixed dynamic range (30 dB).

At peak systole, Fig. 4.2(a) shows strong flow detection in the vessel lumen flow region for the K-means based SVD filter with limited false coloring seen in the vessel wall pixels. Fig. 4.2(b) and (c) show that the frequency and spatial coherence filter achieved comparable performance to the K-means filter in terms of Doppler power detection in the flow regions, whereas Fig. 4.2(d) illustrates that the magnitude filter had very weak flow detection. Another evident finding is that the frequency [Fig. 4.2(b)], spatial coherence [Fig. 4.2(c)] and magnitude filter [Fig. 4.2(d)] power maps all show parallel noise streaks increasing in intensity with depth. However, the noise streaks are very significantly suppressed in the K-means based SVD filter [Fig. 4.2(a)] since the eigen components related to the noise cluster were removed.

At end diastole, Fig. 4.2(e) also shows strong flow detection in the vessel lumen flow region for the K-means based SVD filter with limited false coloring seen in the vessel wall pixels. The frequency and spatial coherence filter in Fig. 4.2(f) and (g) achieved comparable performance to the K-means filter in terms of Doppler power detection in the flow regions, whereas Fig. 4.2(h) shows that the magnitude filter had weak flow detection and strong spurious coloring of vessel wall and

surrounding tissue region. Similar to peak systolic phase, K-means based SVD filter [Fig. 4.2(e)] significantly removed the parallel noise streaks present in the frequency [Fig. 4.2(f)], spatial coherence [Fig. 4.2(g)] and magnitude filter [Fig. 4.2(h)] power Doppler maps.

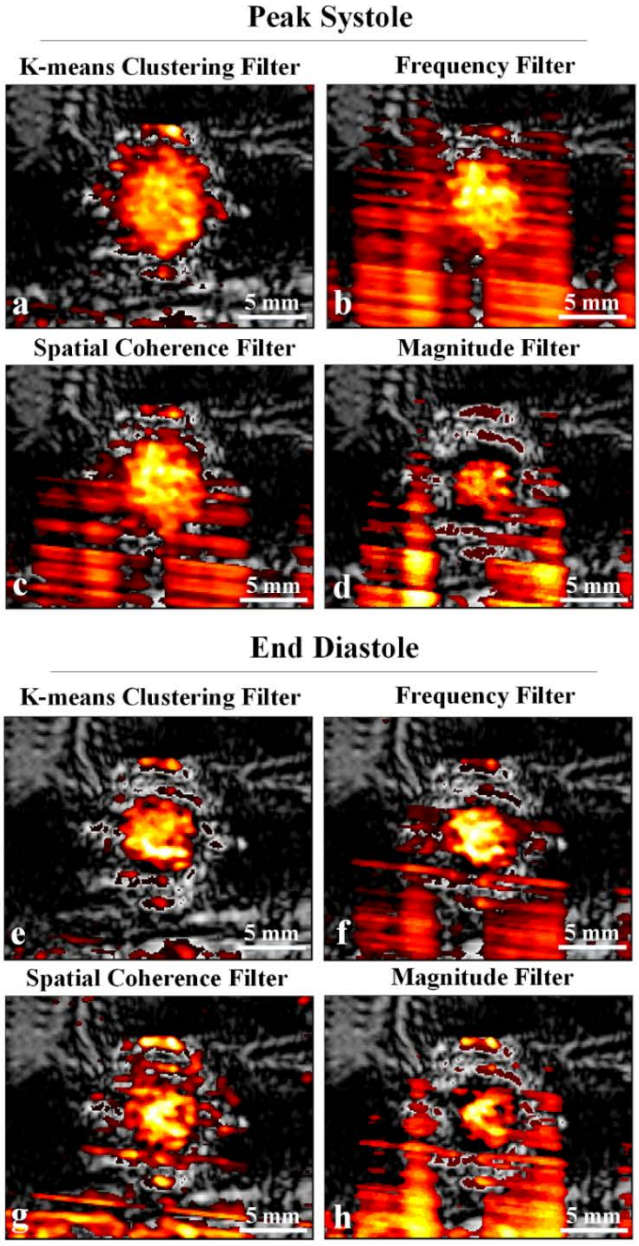

Fig. 4.2. Improved flow detection and noise suppression achieved using (a), (e) K-means based SVD filter in comparison with (b), (f) Frequency based filter, (c), (g) Spatial Coherence based filter, and (d), (h) Magnitude based filter. Post-filtered power Doppler maps overlaid on the flow phantom vessel cross-sectional B-mode image are shown at (a)-(d) peak systole and (e)-(h) end diastole phase of the cardiac cycle. Dynamic range was kept the same for all the images at 30 dB.

4.2.3 Enhanced ROC Performance Gained by K-means Clustering based SVD Filter

The classification performance in ROC analysis can be gauged by the AUC value, the higher it is the better the flow detection. The improved flow detection efficacy of the K-means based SVD filter is statistically substantiated by its high ROC performance as shown in Fig. 4.3. At peak systole, where tissue motion is the strongest due to strong vessel wall pulsations, the ROC curve in red of K-means based SVD filter yielded the largest AUC value (0.98) in comparison to the magnitude filter curve in black (0.73), frequency filter curve in blue (0.90), and the spatial coherence filter curve in green (0.94). At end diastole, where flow and tissue vibration is the slowest, the ROC curve of K-means based SVD filter also yielded the largest AUC value (0.96) in comparison to the magnitude filter curve in black (0.72), frequency filter curve in blue (0.87), and the spatial coherence filter curve in green (0.88). The proposed method also achieved the highest flow detection sensitivity at 10% false alarm rate for both peak systolic and end diastolic phases of the cardiac cycle as evident from Fig. 4.3(a) and (b).

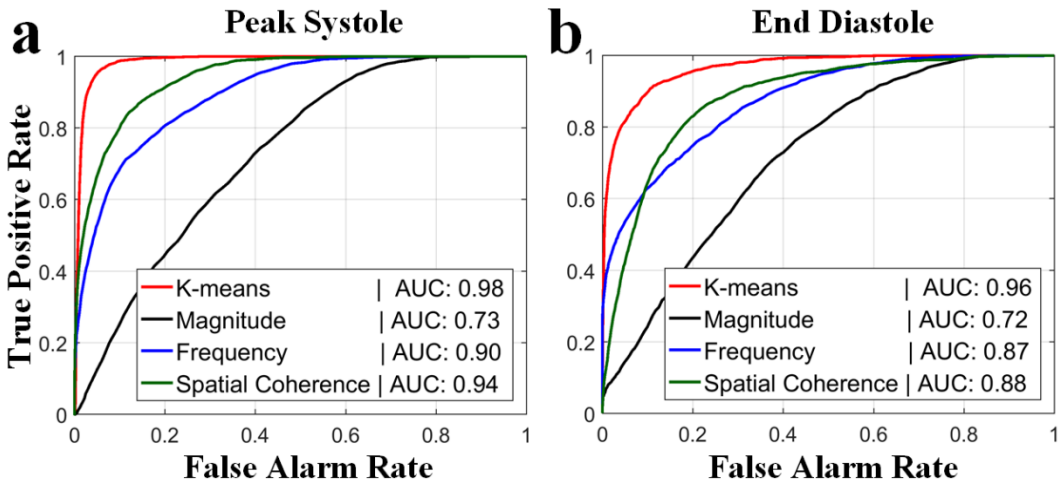

Fig. 4.3. K-means clustering based SVD filter achieved the highest flow detection ROC performance compared to other clutter rank estimation methods at both (a) peak systole and (b) end diastole.

4.2.4 Adaptive Suppression of the Eigen-components Contributes to Improved Clutter Suppression

Fixed eigen thresholds were generated by the magnitude and spatial coherence based filters for removing tissue clutter as shown by their respective dashed lines in Fig. 4.4(a). On the other hand, K-means clustering based SVD filter adaptively detected unwanted eigen components with low blood-to-clutter (BCR) ratio belonging to tissue clutter (blue bars) and noise (black bars). The proposed method also adaptively identified the blood eigen components (red bars) which are otherwise falsely removed as tissue clutter by the magnitude and spatial coherence based estimation approaches.

The spatial eigen images [Fig. 4.4(b) - (g)] served as ground truth to exhibit the actual clutter, blood and noise signal contributions in each selected left (spatial) singular vector. These eigen-images illustrate how K-means based SVD filter correctly identified the eigen components corresponding to tissue clutter [Fig. 4.4(b)], blood [Fig. 4.4(e)] and noise [Fig. 4.4(f)]. Although most of the eigen components were correctly classified by the proposed method, the classification was however not perfect for all eigen components. As shown in Fig. 4.4(c), the 4^{th} spatial (left) singular vector contains weak flow signal in the vessel lumen as well as tissue clutter in the vessel wall region. In this case, since the BCR is relatively higher than the first three clutter components and much lower than the blood components, the correct classification of this 4^{th} left singular vector is challenging due to presence of both clutter and flow signals. Fig. 4.4(d) shows that the 5^{th} left singular vector contains the blood flow signal with high BCR, but the K-means clustering based filter incorrectly classifies this eigen component as clutter. Furthermore, Fig. 4.4(g) shows that the 16^{th} left singular vector comprises of noise signals along with some weak flow signal in the vessel lumen. In this case, since the noise signals are quite significant, K-means classified this eigen component as noise. However, presence of weak blood signal here still makes the correct classification difficult.

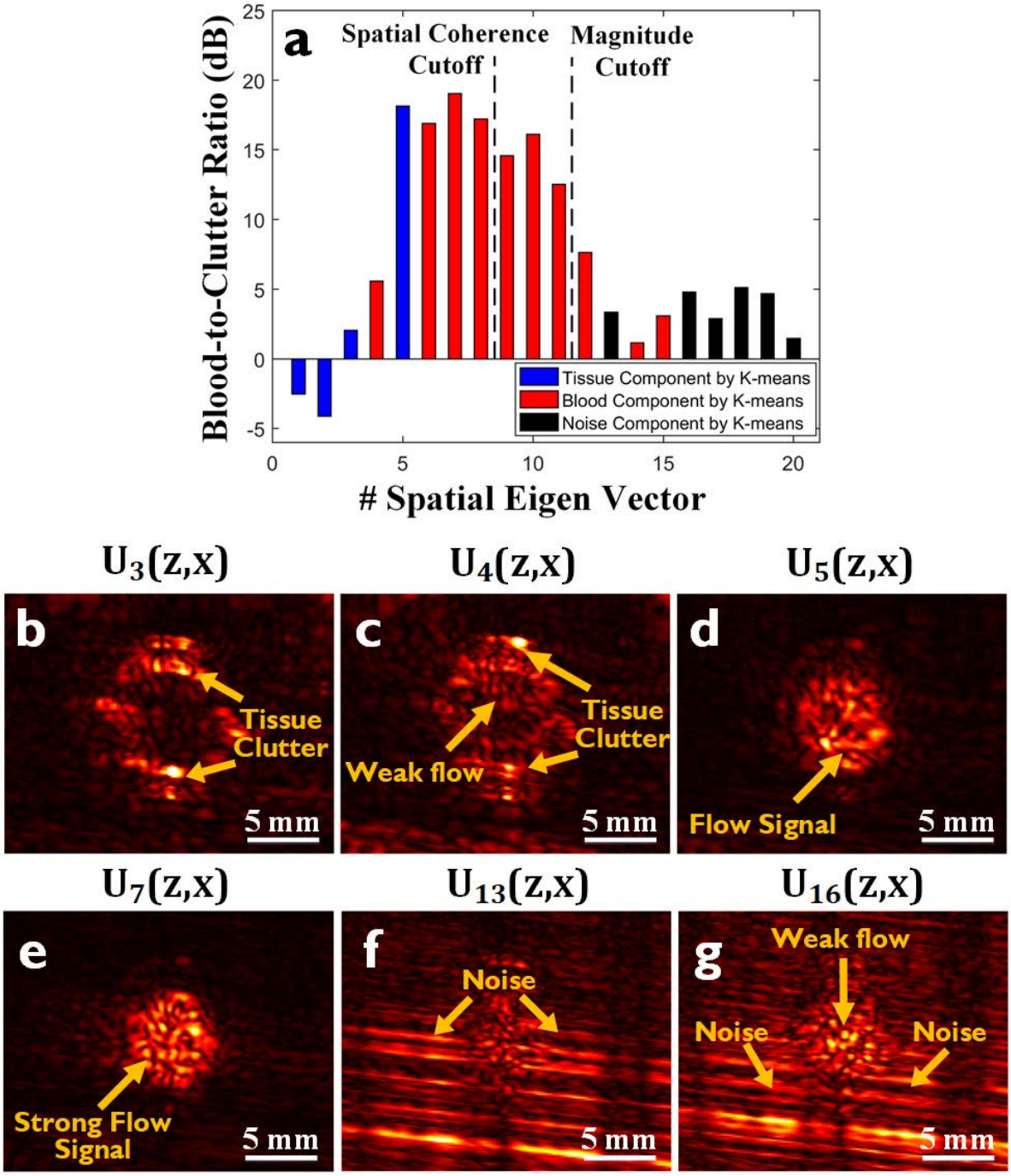

Fig. 4.4. (a) Eigen thresholds (shown in dashed lines) corresponding to tissue clutter computed by Spatial Coherence and Magnitude based clutter rank estimators. Red bars represent the eigen components identified as part of the blood flow signal by the K-means based SVD filter, while the blue bars represent the eigen components identified adaptively as tissue clutter. Black bars represent the eigen components identified by the noise cluster. (b)-(g) Spatial eigen-images from different left singular vectors showing the clutter, blood and noise signal contributions in each.

4.2.5 Effect of "Noise" Cluster Suppression on Flow Detection

Removing the noise cluster identified by the K-means based SVD filter enabled better suppression of the parallel noise streaks present at both peak systolic [Fig. 4.5(a)] and end diastolic [Fig. 4.5(c)] phases of the cardiac cycle. It is evident from both Fig. 4.5(b) and (d) that suppressing the noise cluster had no adverse effect on the Doppler power detected in the flow region. Fig. 4.5(e) shows that at peak systole, noise removal increased the AUC slightly from 0.983 (without noise removal) to 0.986 (with noise removal). Moreover, Fig. 4.5(f) shows a similar trend where noise removal increased the AUC from 0.94 (without noise removal) to 0.96 (with noise removal). Hence, noise suppression yielded a substantial improvement in the flow detection ROC performance at both peak systole [Fig. 4.5(e)] and end diastole [Fig. 4.5(f)], without compromising flow detection accuracy.

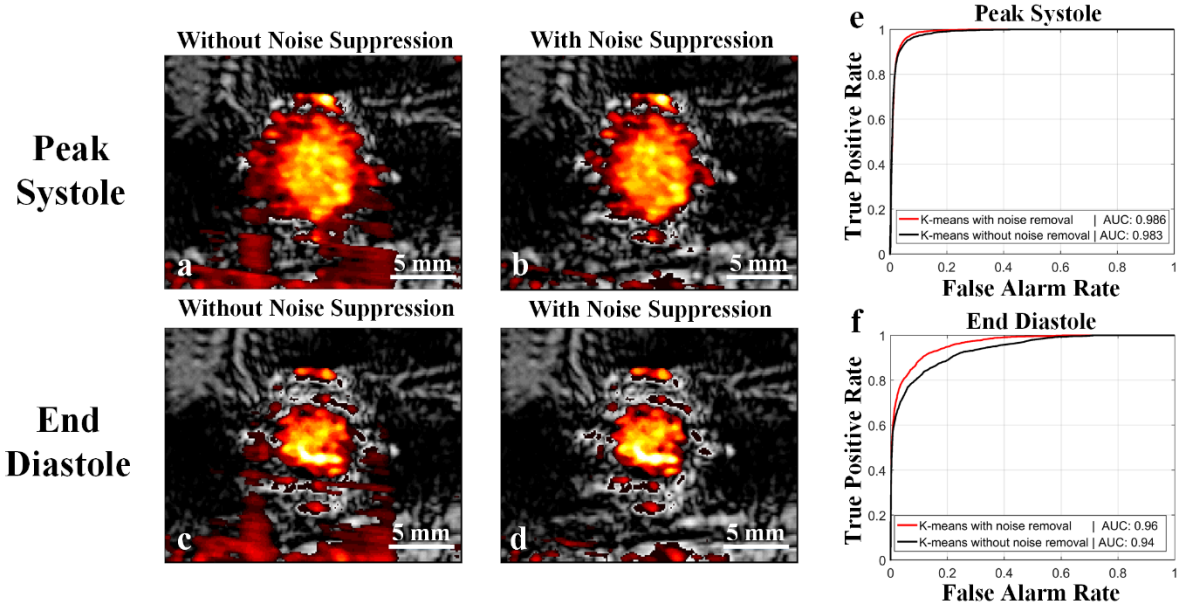

Fig. 4.5. Post-filtered power Doppler map without noise cluster suppression (a) and with noise cluster suppression (b) at peak systole. Post-filtered power Doppler map without noise cluster suppression (c) and with noise cluster suppression (d) at end diastole by the K-means based SVD filter. Comparison of flow detection ROC performance with and without noise removal by the K-means based SVD filter at (e) Peak systole and (f) End Diastole.

4.3 *In vivo* Experimental Results

4.3.1 K-means Clustering Yields Distinct Clusters

K-means clustered the data (convergence time: 17 ms) into discrete groups as shown in Fig. 4.6(a) below. Cluster 1 (blue) has the highest mean singular value magnitude and spatial correlation, and at the same time, the lowest mean Doppler frequency among all, hence cluster 1 can be identified as tissue clutter. Cluster 3 (gray) has the least spatial correlation and the highest frequency content, hence it can be identified as noise. The remaining cluster 2 (red) can therefore be confidently classified as signals from blood flow.

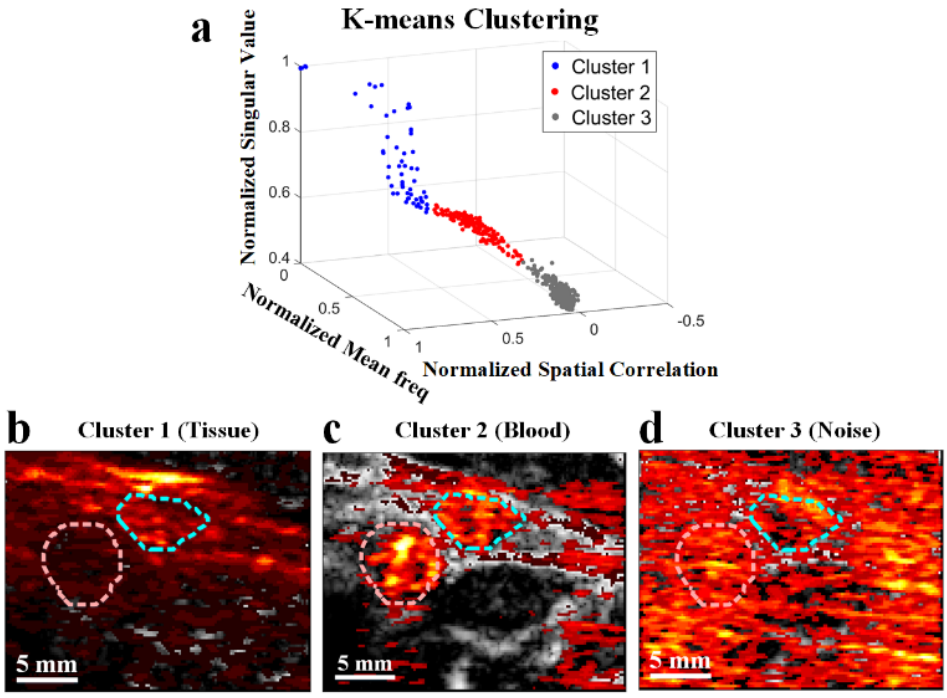

Fig. 4.6. (a) K-means clustering performed on the 3D distribution of image statistics acquired from in-vivo common carotid artery and jugular vein data at peak systolic phase of the cardiac cycle. (b)-(d) Representative spatial eigen-images from each cluster overlaid on B-mode image with lines demarcating the CCA (red dashed circle) and JV (blue dashed circle) flow regions.

The group each cluster belongs to can also be qualitatively identified through its corresponding

spatial eigen-image overlaid on B-mode image for reference. As expected, Fig. 4.6(b) shows the presence of strong vessel wall clutter in the eigen-image from cluster 1. Fig. 4.6(c) clearly shows strong carotid (red dashed circle) and jugular vein (blue dashed circle) blood flow signals along with some noise signals in the spatial eigen-image from cluster 2. The spatial eigen-image from cluster 3 is full of background noise as shown in Fig. 4.6(d).

4.3.2 Strong Flow Detection and Noise Suppression Achieved by the K-means based SVD filter

K-means based clutter filtering strongly differentiated between flow and tissue regions at both diastolic and systolic phase of the cardiac cycle in the presence of strong tissue motion caused by vessel wall pulsations and extrinsic probe motion. Fig. 4.7 shows the post-filtered power Doppler maps at peak systole and end diastole corresponding to different clutter filtering methods which include the K-means based SVD filter [Fig. 4.7(a), (e)], frequency filter [Fig. 4.7(b), (f)], spatial coherence filter [Fig. 4.7(c), (g)], and magnitude filter [Fig. 4.7(d), (h)]. All power maps are rendered with a fixed dynamic range (26 dB).

At peak systole, Fig. 4.7(a) shows strong flow detection in the carotid and vein region for the K-means based SVD filter with limited false coloring seen in the vessel wall pixels. Fig. 4.7(b), (c) and (d) demonstrate that the frequency, spatial coherence and magnitude filter respectively achieved similar performance to the K-means filter in terms of Doppler power detection in the flow regions. Another evident finding is that the frequency, spatial coherence and magnitude filter power maps all show parallel noise streaks increasing in intensity with depth. However, the noise streak is significantly suppressed in the K-means based SVD filter [Fig. 4.7(a)] since the eigen components related to the noise cluster were removed.

At end diastole, Fig. 4.7(e) also shows strong flow detection in the carotid and vein region for the K-means based SVD filter with limited false coloring seen in the vessel wall pixels. The magnitude

and spatial coherence filter in Fig. 4.7(g) and (h) achieved similar performance to the K-means filter in terms of Doppler power detection in the flow regions, whereas Fig. 4.7(f) shows that the frequency filter had very weak carotid flow detection and strong presence of vessel wall clutter. Similar to peak systolic phase, K-means based SVD filter [Fig. 4.7(e)] significantly removed the parallel noise streaks present in the spatial coherence [Fig. 4.7(g)] and magnitude filter [Fig. 4.7(h)] power Doppler maps.

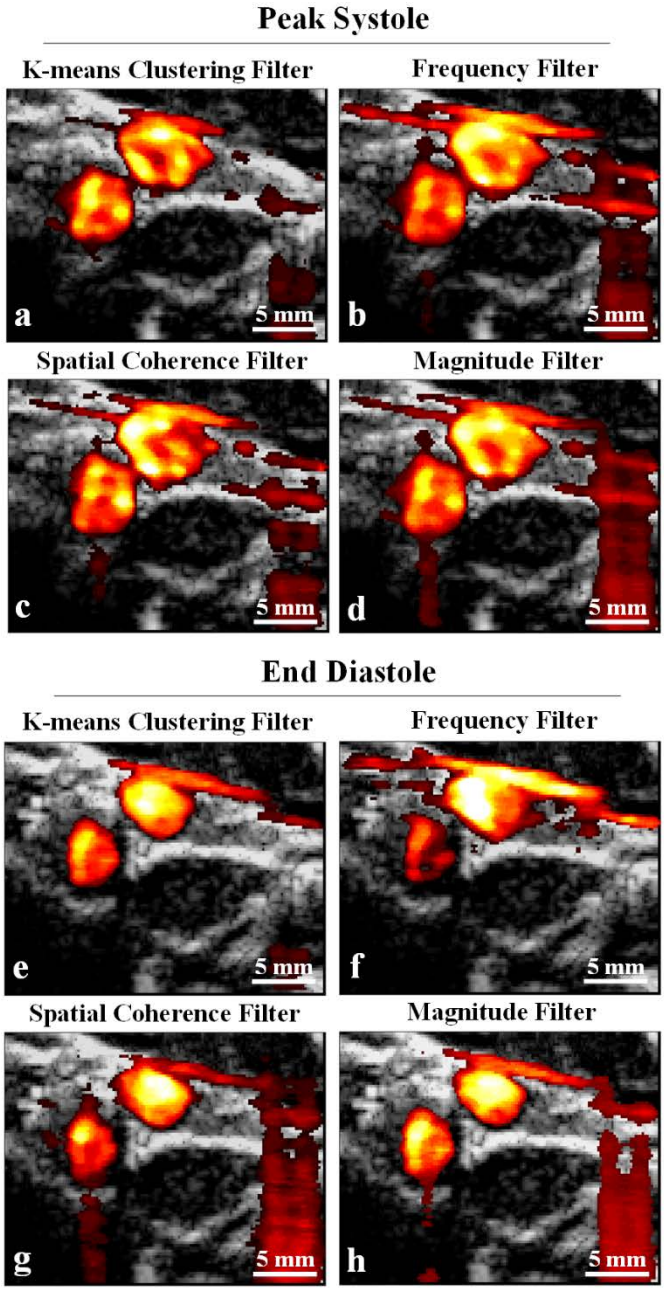

Fig. 4.7. Improved flow detection and noise suppression achieved using (a), (e) K-means based SVD filter in comparison with (b), (f) Frequency based filter, (c), (g) Spatial Coherence based filter, and (d), (h) Magnitude based filter. Post-filtered power Doppler maps overlaid on the CCA and JV cross-sectional B-mode image are shown at (a)-(d) peak systole and (e)-(h) end diastole phase of the cardiac cycle. Dynamic range was kept the same for all the images at 26 dB.

4.3.3 Improved ROC Performance Gained by K-means Clustering based SVD Filter

The improved flow detection efficacy of the K-means based SVD filter is statistically substantiated by its high ROC performance as shown in Fig. 4.8. At peak systole, where tissue motion is the strongest due to strong vessel wall pulsations, the ROC curve in red of K-means based SVD filter yielded the largest AUC value (0.95) in comparison to the magnitude filter curve in black (0.93), frequency filter curve in blue (0.91), and the spatial coherence filter curve in green (0.92). At end diastole, where flow and tissue vibration is the slowest, the ROC curve of K-means based SVD filter also yielded the largest AUC value (0.93) in comparison to the magnitude filter curve in black (0.90), frequency filter curve in blue (0.88), and the spatial coherence filter curve in green (0.89). The proposed method also achieved the highest flow detection sensitivity at 10% false alarm rate for both peak systolic and end diastolic phases of the cardiac cycle as evident from Fig. 4.8(a) and (b).

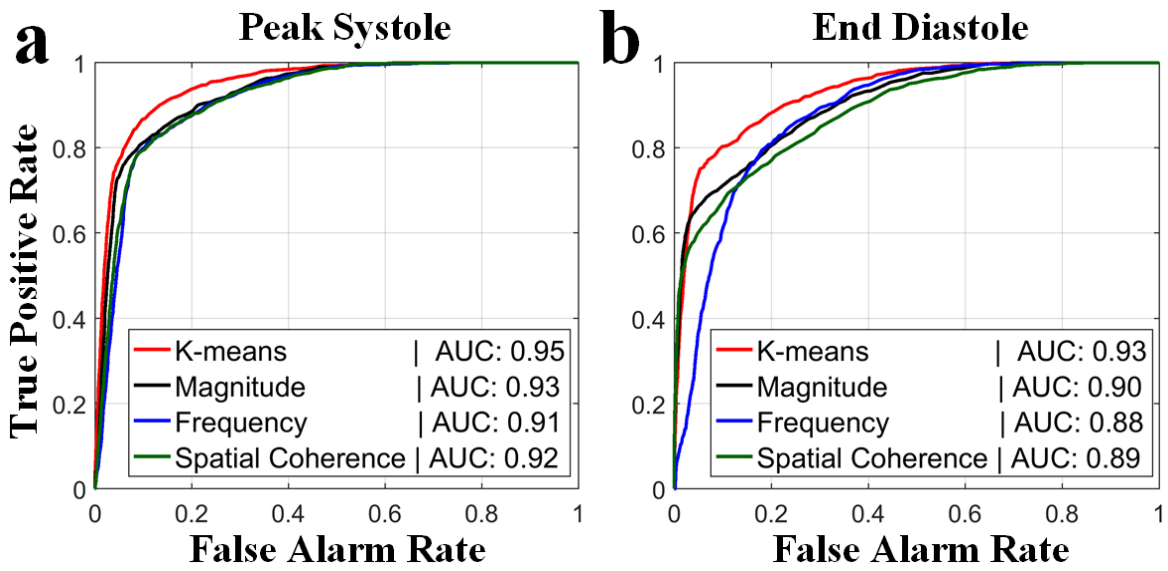

Fig. 4.8. K-means clustering based SVD filter achieved the highest flow detection ROC performance compared to other clutter rank estimation methods at both (a) peak systole and (b) end diastole.

4.3.4 Adaptive Eigen-component Suppression Resulted in Improved Clutter Suppression

Fixed cut-off thresholds were produced by the magnitude and spatial coherence based filters for removing tissue clutter as shown by their respective dashed lines in Fig. 4.9(a). On the other hand, K-means clustering based SVD filter adaptively detected unwanted eigen components with low blood-to-clutter (BCR) ratio belonging to tissue clutter (blue bars) and noise (black bar). The proposed method also adaptively identified the blood eigen components (red bars) which are otherwise falsely removed as tissue clutter by the magnitude and spatial coherence based estimation approaches.

The spatial eigen-images in Fig. 4.9 show how K-means based SVD filter correctly identified the eigen components corresponding to tissue clutter [Fig. 4.9(b)], blood [Fig. 4.9(c)] and noise [Fig. 4.9(e)]. Fig. 4.9(d) shows that the 8^{th} spatial (left) singular vector contains weak carotid and jugular vein flow signals as well as strong tissue clutter in the vein wall region. In this case, since the BCR is relatively higher than the first five clutter components and much lower than the blood components, the correct classification of this 8^{th} left singular vector is challenging due to presence of both clutter and flow signals. However, due to the presence of strong wall clutter, K-means based SVD filter removes this component as tissue clutter.

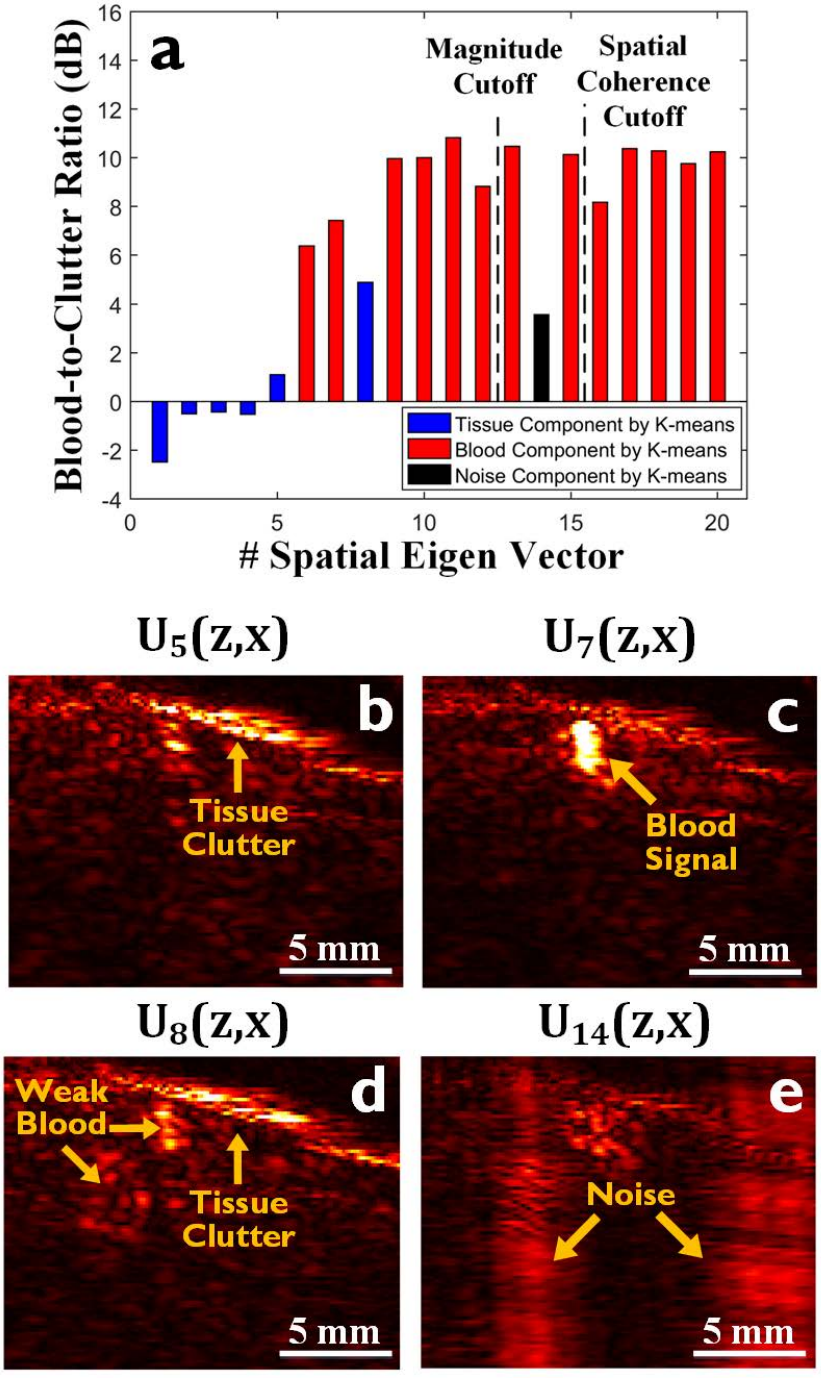

Fig. 4.9. (a) Eigen thresholds (shown in dashed lines) corresponding to tissue clutter computed by Spatial Coherence and Magnitude based clutter rank estimators. Red bars represent the eigen components identified as part of the blood flow signal by the K-means based SVD filter, while the blue bars represent the eigen components identified adaptively as tissue clutter. Black bar represents the eigen component identified by the noise cluster. (b)-(e) Spatial eigen-images from different left singular vectors showing the clutter, blood and noise signal contributions in each.

4.3.5 Effect of "Noise" Cluster Suppression on Flow Detection

Removal of noise cluster classified by the K-means based SVD filter enabled significant suppression of the parallel noise streaks present at both peak systolic [Fig. 4.10(a)] and end diastolic [Fig. 4.10(c)] phases of the cardiac cycle. It is evident from both Fig. 4.10(b) and (d) that suppressing the noise cluster had no adverse effect on the Doppler power detected in the flow regions. Fig. 4.10(e) shows that at peak systole, noise removal increased the AUC from 0.93 (without noise removal) to 0.95 (with noise removal). Moreover, Fig. 4.10(f) shows a similar trend where noise removal increased the AUC from 0.91 (without noise removal) to 0.93 (with noise removal). Hence, noise suppression yielded a considerable improvement in the flow detection ROC performance at both peak systole [Fig. 4.10(e)] and end diastole [Fig. 4.10(f)], without compromising flow detection accuracy.

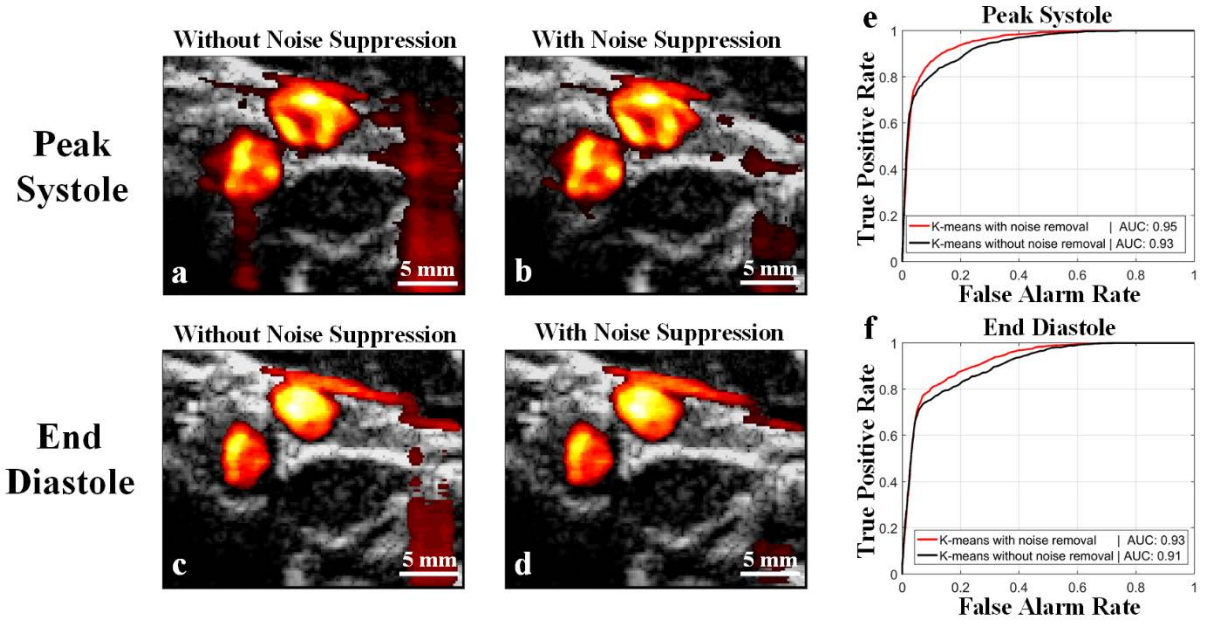

Fig. 4.10. Post-filtered power Doppler map without noise cluster suppression (a) and with noise cluster suppression (b) at peak systole. Post-filtered power Doppler map without noise cluster suppression (c) and with noise cluster suppression (d) at end diastole by the K-means based SVD filter. Comparison of flow detection ROC performance with and without noise removal by the K-means based SVD filter at (e) Peak systole and (f) End Diastole.

Chapter 5 Interpretations and Significance of Study Findings

5.1 Summary of Contributions

Blood flow detection remains a challenging problem in some key clinical scenarios e.g., non-contrast blood perfusion imaging and visualizing blood flow with fast tissue motion. In the presence of tissue motion, clutter echoes become broadband and overlap the slower blood flow signal which makes high-pass filtering based clutter rejection difficult without loss of lower velocity blood flow. Moreover, flow detection performance in eigen filtering suffers if tissue and flow signal subspaces overlap after eigen components are projected to a linear feature space for clutter rank selection. To overcome these limitations, a novel multivariate clustering based eigen-filter design is proposed that robustly detects and removes non-blood eigen components by leveraging on three key spatiotemporal statistics: singular value magnitude, spatial correlation and the mean Doppler frequency of singular vectors. Flow detection performance of the proposed method was evaluated through an *in vitro* flow phantom testbed which exhibited acoustic properties similar to human arteries and soft tissue. Flow detection performance was also tested *in vivo*, where the data characteristics are most realistic.

For both the *in vitro* and *in vivo* experiments, K-means clustering was able to identify distinct clusters corresponding to tissue clutter, blood and noise components in the ultrasound signal. Results showed that the proposed multivariate clustering based SVD filter yielded high flow detection performance in the vessel lumen regions and achieved significant background noise suppression without loss of flow sensitivity. The proposed filter also achieved the highest area under the ROC curve at both peak systole (0.98 for *in vitro*; 0.95 for *in vivo*) and end diastole (0.96 for *in vitro*; 0.93 for *in vivo*) in comparison with other clutter rank estimation methods, signifying its improved flow detection capability. The proposed method was able to adaptively identify and preserve blood eigen components

that were otherwise falsely removed as clutter by the fixed eigen threshold based filters. Furthermore, K-means based SVD filter enabled fully automatic selection of eigen-components that removes dependency on the operator for optimal rank selection.

5.2 Significance of Study Findings

5.2.1 Improved Flow Detection and Noise Suppression Achieved by the K-means based SVD Filter

The post-filtered power Doppler maps for the flow phantom experiment [see Fig. 4.2] and *in vivo* investigation [see Fig. 4.7] have shown the improved performance of K-means based SVD filter in detecting both fast flow at peak systole [Fig. 4.2(a), Fig. 4.7(a)], where the vessel wall motion is very significant, and the slowest flow at end diastole [Fig. 4.2(e), Fig. 4.7(e)], where tissue vibrations also being the slowest result in high spectral overlap between clutter and flow. This demonstrates the enhanced potential of the proposed filter to detect flow in challenging clinical scenarios e.g., detecting slow flow in tumor microvasculature which is critical for cancer diagnoses (Jin, He, Wu, Lin, & Jiang, 2016) and visualizing blood flow with fast tissue motion as in cardiac imaging (Mozumi & Hasegawa, 2019).

Also, the proposed filter concurrently suppressed the spurious noise streaks apparent in the spatial coherence [Fig. 4.2(c), (g); Fig. 4.7(c), (g)], frequency [Fig. 4.2(b), (f); Fig. 4.7(b)] and magnitude filter [Fig. 4.2(d), (h); Fig. 4.7(d), (h)] power Doppler maps. The vessel wall artefact in the power Doppler maps of Fig. 4.7(b), (c), (d) and (f) resulted from angled (-10°) plane wave insonification at right angle to the vessel walls that were well-suppressed in the K-means based SVD power map in Fig. 4.7(a). It is evident from both Fig. 4.5(b), (d) and Fig. 4.7(b), (d) that suppressing the noise cluster had no adverse effect on the Doppler power sensitivity in the flow regions. Noise suppression rather

yielded an improvement in the flow detection ROC performance at both peak systole [Fig. 4.5(e); Fig. 4.10(e)] and end diastole [Fig. 4.5(f), Fig. 4.10(f)], by reducing the spurious coloring of the non-blood pixels and without compromising flow detection accuracy.

5.2.2 Adaptive and Automatic Eigen Rank Estimation

The findings in Fig. 4.4(a) and Fig. 4.9(a) showed that K-means based SVD filter adaptively determines the eigen components corresponding to tissue clutter, blood and noise unlike the magnitude and spatial coherence based rank estimators which select a fixed singular value cut-off for discriminating between tissue clutter and blood flow components. Unwanted eigen components with low blood-to-clutter (BCR) ratio belonging to tissue clutter and noise were also adaptively identified by the proposed method. The spatial eigen images [Fig. 4.4(b) - (g), Fig. 4.9(b) - (e)] served as ground truth to exhibit the actual clutter, blood and noise signal contributions in each selected left (spatial) singular vector. Hence, it is evident from Fig. 4.4 and Fig. 4.9 that adaptive component estimation by the K-means based SVD filter enables significant preservation of blood flow eigen-components that are otherwise falsely removed as tissue clutter by other clutter rank estimation methods. Such adaptive clutter and noise removal allowed the K-means based SVD filter to achieve improved flow detection and noise suppression as demonstrated in Fig. 4.2(a), (e) and Fig. 4.7(a), (e). Furthermore, K-means based SVD filter enabled fully automatic selection of eigen-components that removes dependency on the operator for optimal rank selection.

5.2.3 Highest ROC Performance Achieved by the K-means Based SVD filter

The experimental results for both *in vitro* and *in vivo* experiments are statistically substantiated by the robust ROC performance of the K-means based SVD filter as shown by its red ROC curve yielding the highest AUC value at both peak systole (0.98 for *in vitro* and 0.95 for *in vivo*) [Fig. 4.3(a), Fig. 4.8(a)] and end diastole (0.96 for *in vitro* and 0.93 for *in vivo*) [Fig. 4.3(b), Fig. 4.8(b)] in

comparison to other clutter rank estimators. Both Fig. 4.3 and Fig. 4.8 confirm that, by using K-means based SVD filter, the post-filtered power Doppler values for flow pixels are better distinguished from tissue pixels' values in comparison to rest of the clutter rank estimation techniques.

5.3 Limitations of the Proposed Method

K-means is sensitive to the initial starting positions of cluster centroids. Since the initial cluster center is randomly selected from the data, K-means may produce different results on multiple runs (Celebi, Kingravi, & A.Vela, 2013). Use of an appropriate cluster initialization technique and repeating K-means can help achieve consistent clustering accuracy (Fränti & Sieranoja, 2019). Lastly, CPU-based K-means suffers from a poor convergence time. Such issue can be overcome by parallelized implementation of K-means on a GPU that can speed up the algorithm up to a hundred times faster than CPU-based implementation (Li, Zhao, Chu, & Liu, 2013). Another limitation in the proposed framework is that a slow-time sequence of at least 50 frames is required to have substantial data points available for clustering. This makes the real-time implementation of this framework difficult onto existing clinical scanners which use conventional scan-line based imaging that suffers from limited Doppler ensemble length.

5.4 Future Directions

A direct continuation of this work can be to apply this framework in a block-wise fashion (Song, Manduca, Trzasko, & Chen, 2016) in which SVD is performed on local spatially overlapped segments of the image, rather than applying it globally on the entire image data. This approach can allow more localized extraction of image statistics for clustering which can lead to more robust clutter reduction and potent flow visualization in challenging clinical imaging scenarios. An alternative to K-means is the implementation of deep learning architecture for clustering; deep convolutional networks have demonstrated improved filtering of tissue signal from the ultrasound microbubble signal in

comparison to other iterative methods (Cohen, et al., 2019). To overcome the high computational complexity of SVD and for achieving real-time frame rates, the SVD step in the proposed framework can be parallelized and be implemented on GPU similar to (Chee, Yiu, & Yu, 2017). It has been reported that SVD filter performance increases with the ensemble length (Demené, et al., 2015). Taking advantage of the high frame rates offered by plane wave based ultrasound imaging, effect of using higher Doppler ensemble size on the flow detection performance of the proposed method can be evaluated. This can further aid in the investigation to find potential trade-off between clutter suppression and computation time.

5.5 Research Summary

Tissue clutter is a significant source of artefacts in ultrasound imaging which hampers blood flow detection by dominating part of the blood flow signal in certain challenging clinical imaging applications ranging from cardiac imaging (maximal tissue vibrations) to microvascular flow imaging (very low blood flow speeds). Clutter rank estimation methods based on a single signal feature fail to sufficiently discriminate between tissue clutter and flow subspaces and use a fixed cut-off to distinguish between clutter and blood eigen-components. An improved clutter suppression framework is necessary for HFR ultrasound imaging since it is more susceptible to tissue motion due to poorer spatial resolution.

In this thesis, a novel K-means based SVD filter design is proposed that robustly detects and removes non-blood eigen components by leveraging on three key spatiotemporal statistics: singular value magnitude, spatial correlation and the mean Doppler frequency of singular vectors. Flow detection performance of the proposed method was evaluated *in vitro* through the flow phantom testbed and *in vivo* at the cross-sectional carotid and jugular vein region. K-means based SVD filter was able to identify distinct clusters corresponding to tissue clutter, blood and noise components in the

ultrasound signal. The proposed method was able to adaptively identify and preserve blood eigen components that were otherwise falsely removed as clutter by the fixed eigen threshold based filters. Suppressing the tissue clutter and noise clusters yielded improved flow detection sensitivity and noise rejection in comparison to other eigen-based clutter rank estimation methods. Also, K-means based SVD filter enabled fully automatic selection of eigen-components that removes dependency on the operator for optimal rank selection. The experimental results were statistically substantiated by the robust ROC performance of the proposed method, yielding the highest AUC values at both peak systole (0.98 for *in vitro*; 0.95 for *in vivo*) and end diastole (0.96 for *in vitro*; 0.93 for *in vivo*) in comparison to other clutter rank estimators. The significance of this work is on the automated as well as adaptive (in contrast to a fixed cut-off) selection of eigen-components that may potentially allow to overcome the flow detection challenges associated with cardiac and microvascular flow imaging, and also can enable improved quantification of blood velocities with reduced bias in these clinical applications.

References

Arnal, B., Baranger, J., Demene, C., Tanter, M., & Pernot, M. (2017). In vivo real-time cavitation imaging in moving organs. Physics in Medicine & Biology, 62(3), 843–857.

Arthur, D., & Vassilvitskii, S. (2007). K-means++ : the advantages of careful seeding. ACM-SIAM Symp. on Discrete Algorithms (SODA'07). New Orleans, Louisiana.

Baranger, J., Arnal, B., Perren, F., Baud, O., Tanter, M., & Demené, C. (2018). Adaptive Spatiotemporal SVD Clutter Filtering for Ultrafast Doppler Imaging Using Similarity of Spatial Singular Vectors. IEEE Transactions on Medical Imaging , 37(7), 1574 - 1586.

Bayat, M., & Fatemi, M. (2018). Concurrent Clutter and Noise Suppression via Low Rank Plus Sparse Optimization for Non-Contrast Ultrasound Flow Doppler Processing in Microvasculature. IEEE International Conference on Acoustics, Speech and Signal Processing (ICASSP). Calgary, AB, Canada.

Bayat, M., Fatemi, M., & Alizad, A. (2018). Background Removal and Vessel Filtering of Noncontrast Ultrasound Images of Microvasculature. IEEE Transactions on Biomedical Engineering, 66(3), 831 - 842.

Beevi, S. Z., Sathik, M. M., & Senthamaraikannan, K. (2010). A Robust Fuzzy Clustering Technique with Spatial Neighborhood Information for Effective Medical Image Segmentation. International Journal of Computer Science and Information Security, 7(3), 132-138.

Bjaerum, S., Torp, H., & Kristoffersen, K. (2002). Clutter filter design for ultrasound color flow imaging. IEEE Transactions on Ultrasonics, Ferroelectrics, and Frequency Control, 49(2), 204 - 216 .

C. Tay, P., Acton, S. T., & Hossack, J. A. (2011). A wavelet thresholding method to reduce ultrasound artifacts. Computerized Medical Imaging and Graphics, 35(1), 42-50.

Candès, E. J., Sing-Long, C. A., & Trzasko, J. D. (2013). Unbiased Risk Estimates for Singular Value Thresholding and Spectral Estimators. IEEE Transactions on Signal Processing, 61(19), 4643 - 4657.

Celebi, M. E., Kingravi, H. A., & A.Vela, P. (2013). A comparative study of efficient initialization methods for the k-means clustering algorithm. Expert Systems with Applications, 40(1), 200-210.

Chee, A. J., & Yu, A. C. (2017). Receiver-Operating Characteristic Analysis of Eigen-Based Clutter Filters for Ultrasound Color Flow Imaging. IEEE Transactions on Ultrasonics, Ferroelectrics, and Frequency Control, 65(3), 390 - 399.

Chee, A. J., Ho, C. K., Yiu, B. Y., & Yu, A. C. (2016). Walled Carotid Bifurcation Phantoms for Imaging Investigations of Vessel Wall Motion and Blood Flow Dynamics. IEEE Transactions on Ultrasonics, Ferroelectrics, and Frequency Control, 63(11), 1852 - 1864.

Chee, A. J., Yiu, B. Y., & Yu, A. C. (2017). A GPU-Parallelized Eigen-Based Clutter Filter Framework for Ultrasound Color Flow Imaging. IEEE Transactions on Ultrasonics, Ferroelectrics, and Frequency Control, 64(1), 150 - 163.

Cohen, R., Zhang, Y., Solomon, O., Toberman, D., Taieb, L., Sloun, R. J., & Eldar, Y. C. (2019). Deep Convolutional Robust PCA with Application to Ultrasound Imaging. ICASSP 2019 - 2019 IEEE International Conference on Acoustics, Speech and Signal Processing (ICASSP). Brighton, United Kingdom,.

Demené, C., Deffieux, T., Pernot, M., Osmanski, B.-F., Biran, V., & Gennisson, J.-L. (2015). Spatiotemporal Clutter Filtering of Ultrafast Ultrasound Data Highly Increases Doppler and fUltrasound Sensitivity. IEEE Transactions on Medical Imaging, 34(11), 2271 - 2285.

Dineley, J., Meagher, S., Poepping, T., Dicken, W. M., & Hoskins, P. (2006). Design and characterisation of a wall motion phantom. Ultrasound in Medicine & Biology, 32(9), 1349-1357.

Dolon, L. I., Ghosh, A., Alam, T., Alam, M. S., Khaliluzzaman, M., Imteaj, A., & Hassan, M. M. (2016). Segmentation analysis on magnetic resonance imaging (MRI) with different clustering techniques: Wavelet and BEMD. 2016 International Conference on Innovations in Science, Engineering and Technology (ICISET). Dhaka, Bangladesh.

Fränti, P., & Sieranoja, S. (2019). How much can k-means be improved by using better initialization and repeats? Pattern Recognition, 93, 95-112.

Golfetto, C., Ekroll, I. K., Torp, H. G., & Avdal, J. (2018). 3D Coronary Blood Flow Imaging: A Comparison of Automatic Adaptive Clutter Filters. IEEE International Ultrasonics Symposium (IUS). Kobe, Japan.

Heimdal, A., & Torp, H. (1997). Ultrasound Doppler Measurements of Low Velocity Blood Flow: Limitations Due to Clutter Signals from Vibrating Muscles. IEEE Transactions on Ultrasonics, Ferroelectrics, and Frequency Control, 44(4), 873-881.

Ho, C. K., Chee, A. J., Yiu, B. Y., Tsang, A. C., Chow, K. W., & Yu, A. C. (2017). Wall-Less Flow Phantoms With Tortuous Vascular Geometries: Design Principles and a Patient-Specific Model Fabrication Example. IEEE Transactions on Ultrasonics, Ferroelectrics, and Frequency Control, 64(1), 25 - 38.

Hoeks, A., Vorst, J. v., Dabekaussen, A., Brands, P., & Reneman, R. (1991). An efficient algorithm to remove low frequency Doppler signals in digital Doppler systems. Ultrasonic Imaging, 13(2), 135-144.

Hoskins, P. R., & McDicken, W. (1997). Colour ultrasound imaging of blood flow and tissue motion. The British Journal of Radiology , 70(837), 878-90.

INC, P. (2019, 11 18). Retrieved from Phidgets: https://www.phidgets.com/?tier=3&catid=23&pcid=20&prodid=1029

Jensen, J. (1993). Stationary echo canceling in velocity estimation by time-domain cross-correlation. IEEE Transactions on Medical Imaging, 12(3), 471 - 477.

Jensen, J. A. (2007). Medical ultrasound imaging. Progress in Biophysics and Molecular Biology, 93(1-3), 153-165.

Jensen, J. A., Nikolov, S. I., Gammelmark, K. L., & Pedersen, M. H. (2006). Synthetic aperture ultrasound imaging. Ultrasonics, 44(Supplement), e5-e15.

Jin, Z.-Q., He, W., Wu, D.-F., Lin, M.-Y., & Jiang, H.-T. (2016). Color Doppler Ultrasound in Diagnosis and Assessment of Carotid Body Tumors: Comparison with Computed Tomography Angiography. Ultrasound in Medicine & Biology , 42(9), 2106-2113.

Kadi, A., & Loupas, T. (1995). On the performance of regression and step-initialized IIR clutter filters for color Doppler systems in diagnostic medical ultrasound. IEEE Transactions on Ultrasonics, Ferroelectrics, and Frequency Control , 42(5), 927 - 937.

Kim, M., Abbey, C., Hedhli, J., Dobrucki, L., & Insana, M. (2017). Expanding Acquisition and Clutter Filter Dimensions for Improved Perfusion Sensitivity. IEEE Transactions on Ultrasonics, Ferroelectrics, and Frequency Control, 64(10), 1429 - 1438.

Kruse, D., & Ferrara, K. (2002). A new high resolution color flow system using an eigendecomposition-based adaptive filter for clutter rejection. IEEE Transactions on Ultrasonics, Ferroelectrics, and Frequency Control , 49(12), 1739 - 1754.

Li, Y., Zhao, K., Chu, X., & Liu, J. (2013). Speeding up k-Means algorithm by GPUs. Journal of Computer and System Sciences, 79(2), 216-229.

Lloyd, S. (1982). Least squares quantization in PCM. IEEE Transactions on Information Theory , 28(2), 129 - 137.

Maresca, D., Correia, M., Tanter, M., Ghaleh, B., & Pernot, M. (2018). Adaptive Spatiotemporal Filtering for Coronary Ultrafast Doppler Angiography. IEEE Transactions on Ultrasonics, Ferroelectrics, and Frequency Control, 65(11), 2201 - 2204.

Maresca, D., Correia, M., Villemain, O., Bizé, A., Sambin, L., Tanter, M., . . . Pernot, M. (2018). Noninvasive Imaging of the Coronary Vasculature Using Ultrafast Ultrasound. JACC: Cardiovascular Imaging, 11(6), 798-808.

Montaldo, G., Tanter, M., Bercoff, J., Benech, N., & Fink, M. (2009). Coherent plane-wave compounding for very high frame rate ultrasonography and transient elastography. IEEE Transactions on Ultrasonics, Ferroelectrics, and Frequency Control, 56(3), 489 - 506.

Moubark, A. M., Harput, S., Cowell, D. M., & Freear, S. (2016). Clutter noise reduction in B-Mode image through mapping and clustering signal energy for better cyst classification. IEEE International Ultrasonics Symposium (IUS). Tours, France.

Mozumi, M., & Hasegawa, R. N. (2019). Utilization of singular value decomposition in high-frame-rate cardiac blood flow imaging. Japanese Journal of Applied Physics, 58(SG), SGGE02-1 - SGGE02-8.

Nameirakpam, D., Khumanthem, M., & Jina, C. Y. (2015). Image Segmentation Using K-means Clustering Algorithm and Subtractive Clustering Algorithm. Eleventh International Multi-Conference on Information Processing-2015 (IMCIP-2015), 54. Bangalore, India.

Paul, Y., Barthez, D., DVM, R. L., Peter, V., & Scrivani, D. (1997). Side Lobes and Grating Lobes Artifacts in Ultrasound Imaging. Veterinary Radiology & Ultrasound, 38(5), 387-393.

Pinter, S. Z., & Lacefield, J. C. (2010). Objective Selection of High-Frequency Power Doppler Wall Filter Cutoff Velocity for Regions of Interest Containing Multiple Small Vessels. IEEE Transactions on Medical Imaging, 29(5), 1124 - 1139.

Ramnarine, K. V., Nassiri, D. K., Hoskins, P. R., & Lubbers, J. (1998). Validation of a New Blood-Mimicking Fluid for Use in Doppler Flow Test Objects. Ultrasound in Medicine & Biology, 24(3), 451-459.

So, H., Chen, J., Yiu, B., & Yu, A. (2011). Medical Ultrasound Imaging: To GPU or Not to GPU? IEEE Micro, 31(5), 54 - 65.

Song, F., Zhang, D., & Gong, X. (Dec 2006). Performance evaluation of eigendecomposition-based adaptive clutter filter for color flow imaging. Ultrasonics, 44(Supplement), e67-e71.

Song, P., Manduca, A., Trzasko, J. D., & Chen, S. (2016). Ultrasound Small Vessel Imaging With Block-Wise Adaptive Local Clutter Filtering. IEEE Transactions on Medical Imaging , 36(1), 251 - 262.

Song, P., Trzasko, J., Manduca, A. M., Qiang, B., Kadirvel, R., Kallmes, D. F., & Chen, S. (2017). Accelerated Singular Value-Based Ultrasound Blood Flow Clutter Filtering With Randomized Singular Value Decomposition and Randomized Spatial Downsampling. IEEE Transactions on Ultrasonics, Ferroelectrics, and Frequency Control, 64(4), 706 - 716.

Takahashi, H., Hasegawa, H., & Kanai, H. (June 2015). Echo motion imaging with adaptive clutter filter for assessment of cardiac blood flow. Japanese Journal of Applied Physics, 54(7S1), 07HF09-1 – 07HF09-8.

Tanter, M., & Fink, M. (2014). Ultrafast Imaging in Biomedical Ultrasound. IEEE Transactions on Ultrasonics, Ferroelectrics, and Frequency Control , 61(1), 102 - 119.

Tanter, M., Bercoff, J., Sandrin, L., & Fink, M. (2002). Ultrafast compound imaging for 2-D motion vector estimation: application to transient elastography. IEEE Transactions on Ultrasonics, Ferroelectrics, and Frequency Control, 49(10), 1363 - 1374.

Tierney, J., Coolbaugh, C., Towse, T., & Byram, B. (2017). Adaptive Clutter Demodulation for Non-Contrast Ultrasound Perfusion Imaging. IEEE Transactions on Medical Imaging , 36(9), 1979 - 1991.

Tierney, J., Walsh, K., Griffith, H., Baker, J., Brown, D., & Byram, B. (2019). Combining Slow Flow Techniques With Adaptive Demodulation for Improved Perfusion Ultrasound Imaging Without Contrast. IEEE Transactions on Ultrasonics, Ferroelectrics, and Frequency Control, 66(5), 834 - 848.

Udesen, J., Gran, F., & Jensen, J. A. (2005). Fast color flow mode imaging using plane wave excitation and temporal encoding. Medical Imaging 2005: Ultrasonic Imaging and Signal Processing. 5750, pp. 427-436. San Diego, California, United States: SPIE.

Waraich, S. A., Chee, A., Xiao, D., Yiu, B. Y., & Yu, A. (2019). Auto SVD Clutter Filtering for US Doppler Imaging Using 3D Clustering Algorithm. ICIAR 2019: Image Analysis and Recognition (pp. 473 - 483). Waterloo: Springer, Cham.

Wells, P. N. (2006). Ultrasound imaging. Physics in Medicine & Biology, 51(13), R83 - R98.

Wu, M.-N., Lin, C.-C., & Chang, C.-C. (2007). Brain Tumor Detection Using Color-Based K-Means Clustering Segmentation. Third International Conference on Intelligent Information Hiding and Multimedia Signal Processing . Kaohsiung, Taiwan.

Yiu, B. Y., Tsang, I. K., & Yu, A. C. (2011). GPU-based beamformer: Fast realization of plane wave compounding and synthetic aperture imaging. IEEE Transactions on Ultrasonics, Ferroelectrics, and Frequency Control, 58(8), 1698 - 1705.

Yiu, B. Y., Walczak, M., Lewandowski, M., & Yu, A. C. (2019). Live Ultrasound Color Encoded Speckle Imaging Platform for Real-Time Complex Flow Visualization In Vivo (in press). IEEE Transactions on Ultrasonics, Ferroelectrics, and Frequency Control. doi:10.1109/TUFFC.2019.2892731

Ylitalo, J., & Ermert, H. (1994). Ultrasound synthetic aperture imaging: monostatic approach. IEEE Transactions on Ultrasonics, Ferroelectrics, and Frequency Control, 41(3), 333 - 339.

You, W., & Wang, Y. (Oct 2009). Adaptive clutter rejection for ultrasound color flow imaging based on recursive eigendecomposition. IEEE Transactions on Ultrasonics, Ferroelectrics, and Frequency Control, 56(10), 2217 - 2231.

Yu, A. C., & Cobbold, R. S. (2008). Single-ensemble-based eigen-processing methods for color flow imaging - Part I. The Hankel-SVD filter. IEEE Transactions on Ultrasonics, Ferroelectrics, and Frequency Control , 55(3), 559 - 572.

Yu, A. C., & Lovstakken, L. (2010). Eigen-based clutter filter design for ultrasound color flow imaging: a review. IEEE Transactions on Ultrasonics, Ferroelectrics, and Frequency Control , 57(5), 1096 - 1111.

Yu, A. C., Johnston, K. W., & Cobbold, R. S. (2007). Frequency-based signal processing for ultrasound color flow imaging. Canadian Acoustics, 35(2), 11-23.

Zhang, Y., Gao, Y., Wang, L., Chen, J., & Shi, X. (2007). The Removal of Wall Components in Doppler Ultrasound Signals by Using the Empirical Mode Decomposition Algorithm. IEEE Transactions on Biomedical Engineering, 54(9), 1631 - 1642.

Zweig, M. H., & Campbell, G. (1993). Receiver-operating characteristic (ROC) plots: a fundamental evaluation tool in clinical medicine. Clinical Chemistry, 39(4), 561–577.